Monthly Notices of the ROYAL ASTRONOMICAL SOCIETY

MNRAS **528,** 365–387 (2024) https://doi.org/10.1093/mnras/stae014
Advance Access publication 2024 January 4

The dual role of outflows in quenching satellites of low-mass hosts: NGC 3109

Christopher T. Garling [1]★ Annika H. G. Peter [2] Kristine Spekkens,[3,4] David J. Sand,[5] Jonathan Hargis,[6] Denija Crnojević[7] and Jeffrey L. Carlin[8]

[1]*Department of Astronomy, University of Virginia, 530 McCormick Road, Charlottesville, VA 22904, USA*
[2]*CCAPP, Department of Physics, and Department of Astronomy, The Ohio State University, 191 W. Woodruff Ave., Columbus, OH 43210, USA*
[3]*Department of Physics and Space Science, Royal Military College of Canada, PO Box 17000, Station Forces Kingston, ON K7K 7B4, Canada*
[4]*Department of Physics, Engineering Physics and Astronomy, Queen's University, Kingston, ON K7L 3N6, Canada*
[5]*Department of Astronomy and Steward Observatory, University of Arizona, 933 N. Cherry Avenue, Tucson, AZ 85719, USA*
[6]*Space Telescope Science Institute, 3700 San Martin Drive, Baltimore, MD 21218, USA*
[7]*Department of Physics, University of Tampa, 401 West Kennedy Boulevard, Tampa, FL 33606, USA*
[8]*Rubin Observatory Project Office, 950 N. Cherry Avenue, Tucson, AZ 85719, USA*

Accepted 2024 January 2. Received 2023 December 22; in original form 2023 January 21

ABSTRACT

While dwarf galaxies observed in the field are overwhelmingly star forming, dwarf galaxies in environments as dense or denser than the Milky Way are overwhelmingly quenched. In this paper, we explore quenching in the lower density environment of the Small-Magellanic-Cloud-mass galaxy NGC 3109 ($M_* \sim 10^8$ M$_\odot$), which hosts two known dwarf satellite galaxies (Antlia and Antlia B), both of which are H I deficient compared to similar galaxies in the field and have recently stopped forming stars. Using a new semi-analytic model in concert with the measured star formation histories and gas masses of the two dwarf satellite galaxies, we show that they could not have been quenched solely by direct ram pressure stripping of their interstellar media, as is common in denser environments. Instead, we find that separation of the satellites from pristine gas inflows, coupled with stellar-feedback-driven outflows from the satellites (jointly referred to as the starvation quenching model), can quench the satellites on time-scales consistent with their likely infall times into NGC 3109's halo. It is currently believed that starvation is caused by 'weak' ram pressure that prevents low-density, weakly bound gas from being accreted on to the dwarf satellite, but cannot directly remove the denser interstellar medium. This suggests that star-formation-driven outflows serve two purposes in quenching satellites in low-mass environments: outflows from the host form a low-density circumgalactic medium that cannot directly strip the interstellar media from its satellites, but is sufficient to remove loosely bound gaseous outflows from the dwarf satellites driven by their own star formation.

Key words: galaxies: dwarf – galaxies: evolution.

1 INTRODUCTION

One of the most important questions in galaxy evolution is why galaxies transition from blue and actively star forming to red and quiescent. While quenched high-mass (stellar mass $M_* \geq 10^{11}$ M$_\odot$) galaxies are prevalent in the field, suggesting that they may be quenched by internal mechanisms like feedback from active galactic nuclei and virial shock heating (e.g. Birnboim & Dekel 2003; Di Matteo, Springel & Hernquist 2005; Wang & Abel 2008; Kereš et al. 2009; Martig et al. 2009; Davé, Rafieferantsoa & Thompson 2017; Schreiber et al. 2018), galaxies with lower masses are very rarely observed to be quenched when in isolation (Haines et al. 2007; Geha et al. 2012; Kawinwanichakij et al. 2017). Using catalogues of multiband galaxy photometry derived from wide-field optical imaging surveys, it has been shown that the galactic environment (and in particular, host halo mass) is the primary driver of quenching in these lower mass galaxies (e.g. Woo et al. 2013; Zu & Mandelbaum 2016; Kawinwanichakij et al. 2017; Moutard et al. 2018; Papovich et al. 2018; Davies et al. 2019). This conclusion is consistent with the long-standing observation that red, quenched galaxies are abundant in dense cluster environments (e.g. Dressler 1980; Butcher & Oemler 1984; Hogg et al. 2003; Kauffmann et al. 2004; Cooper et al. 2006; Haines et al. 2007).

Much of the recent progress made in understanding environmental star formation quenching is due to new wide-area surveys that provide data for large statistical samples of galaxies, typically reaching stellar masses of 10^8 M$_\odot$ $\leq M_* \leq 10^{10}$ M$_\odot$ at the faint end (e.g. Driver et al. 2011; Taylor et al. 2011; Chambers et al. 2016; Kuijken et al. 2019; Zou et al. 2019). Below these masses, the study of star formation quenching has mostly been limited to the Local Volume, with particular attention paid to satellites of the Milky Way (MW) and Andromeda (M31). Due to the close proximity of these dwarf satellites, a wide range of observational and theoretical tools can be

★ E-mail: txa5ge@virginia.edu

© 2024 The Author(s).
Published by Oxford University Press on behalf of Royal Astronomical Society. This is an Open Access article distributed under the terms of the Creative Commons Attribution License (https://creativecommons.org/licenses/by/4.0/), which permits unrestricted reuse, distribution, and reproduction in any medium, provided the original work is properly cited.

Downloaded from https://academic.oup.com/mnras/article/528/1/365/7511121 by guest on 08 December 2024

leveraged to learn about their quenching processes (see e.g. Mayer et al. 2006; Grcevich & Putman 2009; Nichols & Bland-Hawthorn 2011; Rocha, Peter & Bullock 2012; Gatto et al. 2013; Slater & Bell 2014; Weisz et al. 2015; Fillingham et al. 2015, 2016, 2019; Wetzel, Tollerud & Weisz 2015; Buck et al. 2019; Digby et al. 2019; Garrison-Kimmel et al. 2019; Akins et al. 2021; Applebaum et al. 2021). These studies indicate that there is a divide in the quenching pathways of the Local Group dwarf satellites around stellar masses of 10^5 $M_\odot$, where the least massive ('ultrafaint') dwarf satellites were quenched by reionization (e.g. Bullock, Kravtsov & Weinberg 2000; Benson et al. 2002; Brown et al. 2014; Weisz et al. 2014, 2015; Rodriguez Wimberly et al. 2019; Sand et al. 2022), while the more massive ('classical') dwarf satellites were quenched later via environmental processes. This later environmental quenching is typically attributed to ram pressure stripping (RPS; Gunn & Gott 1972; Larson, Tinsley & Caldwell 1980) caused by the host's hot gas halo (Gatto et al. 2013; Slater & Bell 2014; Emerick et al. 2016; Fillingham et al. 2016). In particular, the intermediate-mass (10^5 $M_\odot \leq M_* \leq 10^8$ $M_\odot$) dwarf satellites of the MW exhibit short (∼2 Gyr) quenching time-scales that are best explained by direct stripping of the interstellar media of the dwarfs via RPS or tidal stripping (e.g. Fillingham et al. 2015, 2019; Wetzel et al. 2015; Baxter, Cooper & Fillingham 2021). This sort of 'strong' RPS also appears in observations and simulations of dense cluster environments, where RPS is highly effective due to the presence of a hot intracluster medium (e.g. Lotz et al. 2019; Roberts et al. 2019; Tonnesen 2019; Tremmel et al. 2019).

However, the satellites of the MW seem to be somewhat unique in this regard (Geha et al. 2017; Carlsten et al. 2021, 2022; Karunakaran et al. 2021; Mao et al. 2021; Samuel et al. 2022). By comparing star-forming and quenched populations of bright ($M_* \geq 10^8$ $M_\odot$) satellite galaxies measured in wide-area surveys, it has been found that massive dwarfs have longer quenching time-scales (∼4–6 Gyr; Wetzel, Tinker & Conroy 2012; Wheeler et al. 2014). These longer quenching time-scales are consistent with starvation, wherein accretion of gas is ceased after infall to the host but the satellite continues to form stars until its gas reservoir is depleted by star-formation-driven outflows. Quenching via starvation is theorized to require 'weak' environmental RPS, wherein low-density gas at large radii from the dwarf can be removed but the denser interstellar gas of the dwarf cannot (e.g. Maier et al. 2019), such that star formation can continue after infall but gas loosened by stellar feedback (e.g. supernovae) is lost. Thus, both 'strong' RPS and starvation require the presence of a circumgalactic medium (CGM) around the host, given our current theoretical understanding of these quenching mechanisms. Such a CGM could be generated by stellar-feedback-driven gas outflows from the host.

There is an additional factor to be considered when studying environmental quenching that we have so far only mentioned in passing; the dependence of the quenching time-scales and mechanisms on environmental density. Galaxy clusters inhabit the densest environments, while an isolated low-mass galaxy with a few dwarf satellites is a low-density environment. As previously mentioned, quenched dwarf satellites are prevalent in dense environments, while equal-mass dwarfs are predominantly star forming in the field (i.e. when they are far from more massive galaxies; Geha et al. 2012). However, it is unclear how environmental quenching scales to lower host masses.

Such low-density environments are poorly represented in the literature, as the hosts and satellites are intrinsically faint, severely limiting the distances to which such systems can be studied. However, several pioneering surveys have begun to extend the study of environmental quenching to low-density environments (e.g. MADCASH and LBT-SONG; Carlin et al. 2016, 2019, 2021; Garling et al. 2020; Davis et al. 2021), with initial results indicating that such low-mass hosts can, indeed, quench their satellites, with starvation being the most likely quenching mechanism. The theoretical literature considering environmental quenching in low-density environments is similarly sparse, but recent simulations show that these low-mass hosts may be able to sustain hot haloes of circumgalactic gas, which is generally thought to be a requirement for these types of environmental quenching processes (Jahn et al. 2019, 2022). Clearly, our picture of star formation quenching is incomplete, in particular at low satellite and host masses. Additionally, the studies that probe low satellite masses are generally confined to satellites of the MW and M31 and are therefore incomplete in terms of galactic environment; this is a particular problem given that host halo mass is the primary driver of satellite quenching, as mentioned above. As a result, there is much to be gained by extending the study of low-mass ($M_* \leq 10^8$ $M_\odot$) dwarf satellite quenching beyond the MW.

In order to assess the efficacy of different quenching mechanisms in low-density environments, we study the NGC 3109 dwarf association, which is ideal for this kind of study. NGC 3109 itself is similar in stellar mass to the Small Magellanic Cloud (SMC) but has not yet been accreted by a larger galaxy, making this a very low-density environment. NGC 3109 is known to host two classical dwarf analogues, the Antlia and Antlia B dwarf satellite galaxies (see Section 2 for more discussion of the observational properties of the system). NGC 3109 can therefore be considered a dwarf group or association (e.g. Tully et al. 2006; Stierwalt et al. 2015; Pearson et al. 2016).

The Antlia and Antlia B dwarf satellite galaxies both have low present-day H I masses relative to the typical values for isolated dwarfs of similar stellar mass (e.g. Papastergis et al. 2012; Bradford, Geha & Blanton 2015; Scoville et al. 2017), suggesting that they have been affected by environmental quenching. Based on the $M_* - M_{\rm H\,I}$ relation of Bradford et al. (2015), Antlia has only 2 per cent of the H I mass of field dwarfs with comparable stellar mass, while Antlia B has roughly 15 per cent of the H I mass of comparable field dwarfs. While the M_*–$M_{\rm H\,I}$ relation is uncertain at the low-mass end due to the limited sample of low-mass field dwarfs, it is clear that Antlia and Antlia B are significant outliers from the field population, prompting us to examine how their H I could have been depleted.

As the system is nearby (with distance ∼1.3 Mpc; Dalcanton et al. 2009) and well-studied observationally (with measured star formation histories (SFHs) from resolved stellar populations, stellar masses, line-of-sight velocities, etc.), we have excellent data with which to set up a theoretical experiment. These observational data allow us to select analogue dwarf galaxy systems from a cosmological simulation, which we use in concert with a simple semi-analytic model to study the gas mass evolution of the satellites after infall. Through this semi-analytic model we can assess which quenching mechanisms are most important in this system, providing a template that can be applied to other systems to search for a model which is generally successful.

1.1 This approach

We adopt a semi-analytic approach to study satellite quenching in the NGC 3109 system. The primary cosmological ingredient to our analysis is the merger history of NGC 3109; of particular importance is exactly *when* Antlia and Antlia B fell into NGC 3109, because these infall times define the time-scales over which our environmental

Downloaded from https://academic.oup.com/mnras/article/528/1/365/7511121 by guest on 08 December 2024

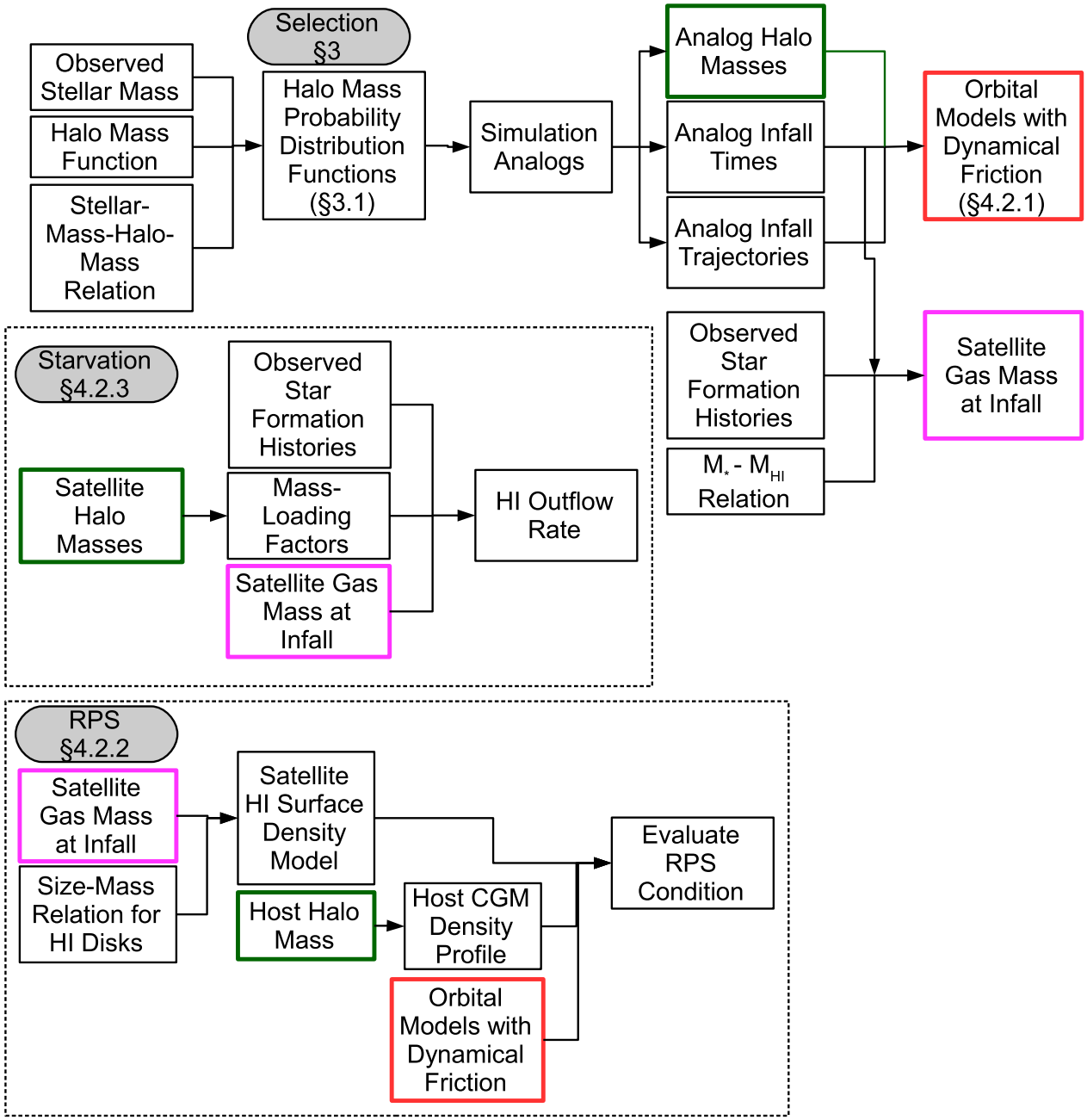

Figure 1. Flow chart summarizing the relationships between different components of our semi-analytic quenching model. We begin at the top of the figure with our selection procedure discussed in Section 3. Coloured boxes indicate intrinsic (e.g. halo masses) or derived (e.g. satellite gas masses at infall) properties of individual analogue systems from the IllustrisTNG simulation that are key inputs to our starvation and RPS quenching models. We then run our semi-analytic quenching model on the analogue systems from the simulation that pass our selection criteria. The relationship between the inputs and outputs for the quenching models are shown in their own labelled flow charts.

quenching models can act. For this purpose, we draw analogues of NGC 3109 and its satellites from big-box hydrodynamic simulations. These simulations are sufficient to resolve the satellites in dark matter, but they generally have poorly resolved baryonic components. As such, it is necessary to post-process the baryonic components of the satellite galaxies, which we accomplish using simple analytic models coupled to the observed SFHs. These theoretical tools, when combined with the observed properties of the NGC 3109 system (e.g. phase-space coordinates, SFHs, and present-day H I gas masses), allow us to discern the most likely quenching pathway for the satellites.

A schematic illustrating how our model operates is shown in Fig. 1. It begins with identifying analogues of the NGC 3109 system that host *either* an Antlia or Antlia B analogue satellite at present day in the simulation. We do not require the system to host *both* an Antlia and an Antlia B analogue; justification for this choice is given in Section 3.3.1. This process relies on the measured stellar masses for each galaxy, which are converted to halo mass probability density functions (PDFs) through a halo mass function (HMF) and an empirical relation between galaxy stellar mass and halo mass; analogues are then selected from the simulation on the

Downloaded from https://academic.oup.com/mnras/article/528/1/365/7511121 by guest on 08 December 2024

Table 1. Assumed properties of the host, NGC 3109, and the satellites, Antlia and Antlia B.

Object	Distance (Mpc)	RA (hms)	Dec. (dms)	M_* (10^5 $M_\odot$)	M_{HI} (10^5 $M_\odot$)	V_{LOS} (km s^{-1})	References
NGC 3109	1.29 ± 0.02	$10^h03^m07^s$	$-26°09'36''$	1400^{+400}_{-300}	3800 ± 500	405 ± 2	(1) (1) (1) (2) (3) (4)
Antlia	1.29 ± 0.02	$10^h04^m04^s$	$-27°19'55''$	73 ± 9	6.8 ± 1.4	363 ± 2	(1) (1) (1) (5) (3) (4)
Antlia B	1.35 ± 0.06	$09^h48^m56^s$	$-25°59'24''$	6^{+4}_{-3}	2.8 ± 0.2	376 ± 2	(6) (7) (7) (7) (7) (7)

References: (1) Dalcanton et al. (2009); (2) Cook et al. (2014); García-Benito et al. (2019); (3) Barnes & de Blok (2001); (4) Ott et al. (2012); (5) McQuinn et al. (2010b); (6) Hargis et al. (2020); (7) Sand et al. (2015).

basis of halo mass. The process of analogue selection is explained in Section 3.

From these simulated analogues we establish the initial conditions for our semi-analytic models by incorporating other empirical and theoretical relations (Section 4.1). The stellar mass of the analogue satellites at infall is set by integrating the observational SFHs for the real satellites up until infall. We then use the empirical relation between stellar mass and H I mass for isolated dwarfs to set the H I mass of the satellites at infall, which is used for both the RPS (Section 4.2.2) and starvation (Section 4.2.3) calculations. For starvation, the only other important variable quantity is the effective mass-loading factor, which is the constant of proportionality between the star formation rate and the star-formation-driven H I mass outflow rate (i.e. η such that $dM_{HI}/dt \propto -\eta\, dM_*/dt$). This mass-loading factor can generally be tied to the halo mass of the satellite. Coupling the initial satellite H I mass, mass-loading factor, observed SFH, and infall time gives us enough information to calculate the gas mass-loss rate due to starvation.

For RPS, we require a few more components. As RPS is dependent on the satellite orbits, and the time resolution of the simulation output is poor, we resimulate the orbits of the satellite analogues with dynamical friction as discussed in Section 4.2.1. RPS is also dependent on the satellite gas surface density profile, which we couple to the initial H I mass following relations from the literature. The density profile of the host CGM is also important, for which we adopt a literature relation tied to the host halo mass. Given the satellite orbit and the gas profiles of the host and satellite, we can determine how much gas is removed by RPS after infall of the analogue satellites. Due to our semi-analytic method, we are able to separate the effects of starvation and RPS to determine which is more effective.

In Section 5, we present results from the fiducial model and explore tidal stripping, alternate quenching model parameters, and uncertainties in the quenching models. Our model clearly indicates that starvation is more effective at removing gas from satellites of low-mass hosts than RPS. We further show that our fiducial RPS model, in the absence of starvation, produces Antlia and Antlia B analogues that are too gas-rich across the entire range of infall time of our simulated analogues, indicating the importance of starvation for quenching such satellites of low-mass hosts. We comment on the implications of this result in Section 6.

2 OBSERVATIONAL PROPERTIES

One of the principle reasons for using the NGC 3109 system as a case study for quenching in low-mass systems is the abundance of data available for the host and satellites, including stellar masses, SFHs, and H I masses. In this section, we highlight the observational properties that will be relevant for our theoretical work. These quantities are also presented in Table 1.

The primary observable we use to select analogues from the simulations are the observed stellar masses for NGC 3109 and its satellites (see Section 3 for a discussion of our selection procedure). We adopt a stellar mass of $7.3 \pm 0.9 \times 10^6$ $M_\odot$ for the Antlia dwarf satellite based on its resolved SFH (McQuinn et al. 2010a, b). Thus, Antlia sits at the upper end of the classical dwarf regime, with a stellar mass within an order of magnitude of the Leo I, Fornax, and Sculptor dwarf satellites of the MW (McConnachie 2012, and references therein). For the Antlia B dwarf satellite, we adopt $6^{+4}_{-3} \times 10^5$ $M_\odot$ for its stellar mass, based on the aperture photometry of Sand et al. (2015). This work assumed a stellar mass-to-light ratio of $\Upsilon = 1$. This also makes Antlia B a classical dwarf analogue, with a stellar mass comparable to the Draco, Ursa Minor, Sextans I, Carina, Canes Venatici I, and Leo II dwarf satellites of the MW (McConnachie 2012).

It is worth noting that the stellar mass of NGC 3109 is significantly uncertain; McConnachie (2012) lists 7.6×10^7 $M_\odot$ and cites Blais-Ouellette, Amram & Carignan (2001), who fit the stellar mass-to-light ratio of NGC 3109 to their H I radial velocity profile under several different models for the halo density profile. However, these stellar-mass-to-light ratios have an order of magnitude spread depending on which halo profile is considered, and several of these profiles have similar goodness of fit. We derive the stellar mass of NGC 3109 by adopting photometry from Cook et al. (2014), which is more precise than the photometry used in Blais-Ouellette et al. (2001), and estimate the stellar-mass-to-light ratio using the colour-dependent relationships in García-Benito et al. (2019). Using this method, we find a stellar mass-to-light ratio of $\Upsilon = 0.8$, which implies a stellar mass of 1.4×10^8 $M_\odot$. Adopting the lognormal spread of 0.11 dex in the colour-stellar-mass-to-light ratio from García-Benito et al. (2019), the $1-\sigma$ range of stellar masses is 1.1×10^8 to 1.8×10^8 $M_\odot$. These estimates are roughly twice the value of 7.6×10^7 $M_\odot$ from McConnachie (2012) and Blais-Ouellette et al. (2001), but are based on better photometry (Cook et al. 2014) and stellar mass-to-light ratios (García-Benito et al. 2019).

We can additionally compare to the K_s band luminosity, which has a fairly constant stellar-mass-to-light ratio of 0.6 with $\sim$0.1 dex scatter (McGaugh & Schombert 2014). Adopting the K_s mag from the 2-Micron All-Sky Survey Large Galaxy Atlas (Jarrett et al. 2003) we find a stellar mass of 2.4×10^8 M_*, with a 1σ range of 1.9×10^8 to 3.0×10^8 M_*. This is higher than the estimate from the optical photometry, but they agree at a 1.2σ level and both prefer a higher stellar mass than that given in McConnachie (2012) and Blais-Ouellette et al. (2001). Both the optical (Cook et al. 2014) and infrared (Jarrett et al. 2003) magnitudes were corrected for Galactic extinction using the Cardelli, Clayton & Mathis (1989) extinction law and the Schlegel, Finkbeiner & Davis (1998) dust maps with the updated scaling from Schlafly & Finkbeiner (2011).

Our revised stellar mass estimates from the optical (Cook et al. 2014) and infrared (Jarrett et al. 2003) photometry are sufficiently consistent that it makes no significant difference to our conclusions

Downloaded from https://academic.oup.com/mnras/article/528/1/365/7511121 by guest on 08 December 2024

in Section 5 which we use. We adopt the stellar mass estimate for NGC 3109 based on the Cook et al. (2014) magnitudes and García-Benito et al. (2019) stellar mass-to-light ratio for our analysis. This stellar mass is comparable to that of the SMC (McConnachie 2012). We note that RPS is more effective for larger host stellar masses, so by assuming a larger stellar mass for NGC 3109 we are making RPS more effective than it would be if we adopted the Blais-Ouellette et al. (2001) stellar mass.

While the present-day stellar masses of the satellite galaxies are important for selecting analogues from the cosmological simulation (Section 3), how the satellites built up their stellar masses over time (i.e. their SFHs) matters for our implementation of quenching via starvation (Section 4.2.3). Normally in fully semi-analytic models, the SFH of galaxies is self-consistently evolved depending on other variables like neutral or molecular hydrogen masses. For a case-study like this, such an approach is undesirable because the real satellites have a fixed intrinsic SFH which may not be well-sampled by the simulated analogues. Fortunately, both Antlia and Antlia B have measured SFHs based on resolved stars. We therefore adopt these SFHs directly (from Weisz et al. 2011 for Antlia and Hargis et al. 2020 for Antlia B) so that the SFH is not a free parameter in our model. These SFHs are utilized in our model of starvation, wherein stellar feedback from young stars (primarily in the form of supernovae) ejects gas from the satellite, slowly quenching its star formation after infall as (under the model assumptions) the satellite cannot accrete more gas from its environment while inside the halo of NGC 3109. The SFHs of both Antlia and Antlia B show little star formation in the last few Gyr, suggesting that some environmental quenching process is responsible.

The measured H I masses of Antlia and Antlia B are also suggestive of environmental effects, as they are lower than those of isolated dwarfs in the field of similar stellar mass (e.g. Papastergis et al. 2012; Bradford et al. 2015; Scoville et al. 2017). Typically such isolated dwarfs have at least twice as much mass in H I as in stars, but this is not the case for the dwarf satellites of NGC 3109. Antlia has a measured H I mass of $6.8 \pm 1.4 \times 10^5$ $M_\odot$ (Barnes & de Blok 2001), roughly 10 per cent of its stellar mass, while Antlia B has an H I mass of $2.8 \pm 0.2 \times 10^5$ $M_\odot$ (Sand et al. 2015), which is roughly half of its stellar mass.

With the measured H I masses, we also get line-of-sight velocities for the dwarfs (Barnes & de Blok 2001; Ott et al. 2012; Sand et al. 2015), which we use in concert with the two-dimensional (2D) separation in the plane of the sky between NGC 3109 and its satellites to further constrain our simulated samples (see Section 3.3 and Appendix A). While NGC 3109, Antlia, and Antlia B all have robust distance measurements that indicate they are associated (Dalcanton et al. 2009; Hargis et al. 2020), the uncertainties are still large enough that there is little to be gained (in a statistical sense) from including the distances of the galaxies into these constraints.

3 SIMULATIONS

We use simulations to select an ensemble of NGC 3109-like analogues, the key input for our semi-analytic quenching exploration. Simulations allow us to sample the range of satellite infall times and orbits that are consistent with the observed properties of the satellites (e.g. their angular separation and relative line-of-sight velocity from the host). Infall times matter because they set the clock for the time-scale of quenching, and the orbits matter because RPS is orbit-dependent. Applying the same semi-analytic model across the sample of analogue systems yields a statistical exploration of quenching mechanisms and time-scales. With the probabilistic analogue selection procedure we describe below, we can more accurately examine the probability distributions of quantities like the satellite infall times and the H I mass-loss due to RPS.

We utilize the public IllustrisTNG cosmological simulations to select analogues of the NGC 3109 system (Marinacci et al. 2018; Naiman et al. 2018; Nelson et al. 2018; Springel et al. 2018; Pillepich et al. 2018b). IllustrisTNG is simulated with a Lambda cold dark matter (ΛCDM) cosmology with parameters from the Planck 2015 results ($h = 0.6774$; Planck Collaboration XIII 2016); we will adopt this cosmology throughout. IllustrisTNG includes hydrodynamics, with a fiducial physics model presented in Weinberger et al. (2017) and Pillepich et al. (2018a). We use the TNG100 run, which simulates a comoving box of volume 110.7 Mpc^3 with 1820^3 particles each for dark matter and gas and twice as many tracers that are used to track the Lagrangian evolution of the gas (Genel et al. 2013). This simulation suite is well-matched to our science goals, because it has sufficiently high resolution in dark matter over a sufficiently large volume for us to obtain a statistically significant set of NGC 3109 system analogues.

We utilize the friends-of-friends (FoF) group catalogues to identify isolated host systems, the SUBFIND subhalo catalogues to extract subhalo properties, and the SUBLINK merger trees (Rodriguez-Gomez et al. 2015) to track the evolution of the subhaloes through time. The FoF halo finder requires a minimum of 32 particles, corresponding to 2.4×10^8 $M_\odot$ if the particles are all dark matter, while SUBFIND requires a minimum of 20 particles that are gravitationally bound, corresponding to a halo mass lower bound of 1.5×10^8 $M_\odot$. In Section 3.1, we show that the expected halo mass for Antlia B, the least massive galaxy in the NGC 3109 system, is a factor of 20 larger than this, giving us confidence that the dark matter haloes of satellites like Antlia and Antlia B in the simulation will be sufficiently resolved for our purposes (see Fig. 1 for an overview of how we use the halo quantities from the simulation).

To define a set of analogues, the principal observables we have for NGC 3109 and its satellites are their stellar masses (see Table 1). The easiest way to identify analogueous systems in TNG100 would be to find systems with similar stellar masses in the simulation catalogues. However, the baryonic particle masses in TNG100 are 1.4×10^6 $M_\odot$, so that the stellar masses of Antlia and Antlia B analogues will be poorly resolved. Instead, we can infer the halo masses of NGC 3109 and its satellites from their stellar masses given a stellar-mass–halo-mass (SMHM) relation, an HMF, and a subhalo mass function (SMF). The conversion of observed stellar mass to approximate halo mass must be considered carefully. As noted in Dooley et al. (2017), Somerville et al. (2018), Jethwa, Erkal & Belokurov (2018), and other works, the SMHM relation cannot simply be inverted to obtain a halo mass from an observed stellar mass because the relationship has intrinsic scatter. This leads to significant Eddington bias, as there are many more low-mass galaxies to be up-scattered than high-mass galaxies to be down-scattered, indicating that a naive inversion of the SMHM relation would overestimate the typical halo mass of galaxies observed at a fixed M_*. This effect can be mitigated by including models for the HMF and SMF as shown below.

3.1 Selection of analogues via halo mass probabilities

The PDF of a halo mass given a stellar mass, $P(M_\mathrm{h}|M_*)$ can be related to the PDF of a stellar mass given a halo mass from the SMHM relation, $P(\mathrm{M}_*|M_\mathrm{h})$, and the HMF, $\mathrm{d}N/\mathrm{d}M_\mathrm{h} \propto P(\mathrm{M}_h)$, through Bayes' theorem as $P(M_\mathrm{h}|M_*) \propto P(M_*|M_\mathrm{h})\,P(M_\mathrm{h})$. We additionally add a reionization quenching model that describes the fraction of haloes of mass M_h that are luminous, denoted $f_\mathrm{lum}(M_\mathrm{h})$. For a constant

Downloaded from https://academic.oup.com/mnras/article/528/1/365/7511121 by guest on 08 December 2024

lognormal scatter in the SMHM relation in dex of σ and a fiducial stellar mass of M_*, we can write the PDF of a stellar mass given a halo mass as

$$P(M_*|M_\mathrm{h}) = \frac{f_\mathrm{lum}(M_h)}{M_*\,\sigma\,\ln 10\,\sqrt{2\pi}} \times \exp\left[\frac{-\left(\log_{10}M_* - \log_{10}\mathrm{SMHM}\,(M_\mathrm{h})\right)^2}{2\sigma^2}\right], \quad (1)$$

where SMHM(M_h) is the median stellar mass from the SMHM relation for a halo mass of M_h. In order to apply Bayes' theorem to find $P(M_\mathrm{h}|M_*)$ we must calculate the Bayesian evidence to properly normalize the PDF, which can be written as

$$A = \int_0^\infty \int_0^\infty P(M_*|M_\mathrm{h})\,\frac{\mathrm{d}N}{\mathrm{d}M_h}\,P(M_*)\,\mathrm{d}M_\mathrm{h}\,\mathrm{d}M_*, \quad (2)$$

where $P(M_*)$ is the PDF for the stellar mass of the object in question. We can then write the conditional PDF of M_h given M_* as

$$P(M_\mathrm{h}|M_*) = \frac{1}{A}\int_0^\infty P(M_*|M_\mathrm{h})\,\frac{\mathrm{d}N}{\mathrm{d}M_h}\,P(M_*)\,\mathrm{d}M_*. \quad (3)$$

One useful application of this equation is to compute the expectation value for the halo mass of a galaxy given its stellar mass, which can be written as

$$\langle M_\mathrm{h}\rangle = \int_0^\infty \int_0^\infty M_\mathrm{h}\,P(M_\mathrm{h}|M_*)\,\mathrm{d}M_\mathrm{h}\,\mathrm{d}M_* = \frac{1}{A}\int_0^\infty \int_0^\infty M_\mathrm{h}\,P(M_*|M_\mathrm{h})\,\frac{\mathrm{d}N}{\mathrm{d}M_\mathrm{h}}\,P(M_*)\,\mathrm{d}M_\mathrm{h}\,\mathrm{d}M_*. \quad (4)$$

When considering the halo mass PDFs for subhaloes, the SMF, $\mathrm{d}N/\mathrm{d}M_{\mathrm{h,sat}}(M_{\mathrm{h,host}})$, should be used instead of the HMF. We use the form of the HMF from Sheth, Mo & Tormen (2001) with the transfer function from Eisenstein & Hu (1999) to generate the HMF, the SMF and $f_\mathrm{lum}(\mathrm{M}_h)$ from Dooley et al. (2017), and the Moster, Naab & White (2013) SMHM relation. We assume a constant 0.2 dex scatter in stellar mass at fixed M_h (e.g. Behroozi, Wechsler & Conroy 2013; Dooley et al. 2017). There is evidence for increased scatter in the SMHM below $M_\mathrm{h} \sim 10^{11.5}\,\mathrm{M}_\odot$, but we choose to keep a constant scatter for easier comparison to other work. The expected M_h derived from equation (4) are typically $\sim$ 10 per cent lower than the result from a simple inversion of the Moster et al. (2013) SMHM relation in the range of stellar mass considered here.

With PDFs for the halo masses of NGC 3109 and its satellites, we are able to select halo mass ranges for each based on percentiles of enclosed probabilities, e.g. 68 per cent corresponding to the 1σ range for a Gaussian distribution. It is typical when selecting analogues of observational systems from simulations to choose a narrow range around the expected halo mass and approximate all simulated analogues as being equally likely to represent the observed system. However, this approach both limits the sample size of simulated analogues and neglects the tails of the halo mass PDF. We instead derive analogue halo mass selection ranges as the intervals that contain 99.7 per cent of the probability from the full halo mass PDFs (equivalent to $\pm 3\sigma$ for a Gaussian distribution), and fully propagate the probability that each simulated system represents the observed system through our analysis. We present our expectation values for M_h and selection ranges in Table 2, along with the results from a naive inversion of the SMHM relation for comparison.

Table 2. The expectation values of $M_{200\mathrm{c}}$ and infall mass selection ranges for analogues from IllustrisTNG derived from equation (4), compared to the expectations from a naive inversion of the SMHM relation neglecting scatter. The selection ranges enclose 99.7 per cent of the halo mass PDFs.

Object	$\langle M_{200\mathrm{c}}\rangle$ ($10^9\,\mathrm{M}_\odot$)	Naive inversion ($10^9\,\mathrm{M}_\odot$)	Lower limit ($10^9\,\mathrm{M}_\odot$)	Upper limit ($10^9\,\mathrm{M}_\odot$)
NGC 3109	38.7	43.0	19.2	69.3
Antlia	10.8	12.2	5.70	19.2
Antlia B	3.12	4.26	1.26	8.13

3.2 Halo overdensity definitions

There is an additional complication here related to the definition of the halo mass. This matters because we match the stellar and dark matter halo masses of satellites at the time of satellite infall, and because Antlia is a major merger event for NGC 3109. Often halo masses are defined relative to spherical overdensity (SO) criteria; e.g. $\mathrm{M}_{200\mathrm{c}}$ is defined to be the total halo mass enclosed in a sphere whose average density is 200 times the critical density of the Universe, with a corresponding radius $R_{200\mathrm{c}}$. Such SO masses and radii are only calculated in IllustrisTNG for the FoF group catalogues, while the SUBFIND subhalo catalogues and SUBLINK merger trees contain no such quantities, having instead only total gravitationally bound masses; these are not directly comparable to SO quantities. Generally, models of the type used in equation (3) are expressed in terms of SO mass definitions, with $M_{200\mathrm{c}}$ being the most common mass definition – we adopt $M_{200\mathrm{c}}$ to evaluate equation (3), as all of the component models support this definition. Given that the stellar masses of satellites are more closely tied to their halo masses at infall than at present day (e.g. Reddick et al. 2013; Rodríguez-Puebla et al. 2017; Campbell et al. 2018; Behroozi et al. 2019; Buck et al. 2019; Moster et al. 2021; Wang et al. 2021), what we would like in order to perform our analogue selections are present-day $M_{200\mathrm{c}}$ values for the hosts, and $M_{200\mathrm{c}}$ values at infall for the satellites.

The obvious choice would be to use the $M_{200\mathrm{c}}$ values from the FoF catalogues for the hosts at present day, but these will include the masses of all subhaloes. This is normally fine in the limit of $M_\mathrm{host} >> M_\mathrm{sat}$, but given that Antlia is expected to have a halo mass $\sim$ 25 per cent that of NGC 3109 (i.e. Antlia's infall constitutes a major merger), using these FoF masses for the hosts may bias our host selection as the FoF masses are correlated with the total mass in substructure. Instead, we identify the most massive subhalo in the SUBFIND catalogues to be the central subhalo for a given satellite's FoF group. The subhalo mass for the central will consider particles that are only bound to the central and no other substructure, allowing us to avoid this bias. In order to convert the SUBFIND subhalo mass to an SO mass, we approximate $M_\mathrm{SUBFIND} \approx M_{150\mathrm{c}}$. Prior to Antlia's infall, we find good agreement between the FoF $M_{200\mathrm{c}}$ values and those obtained by this approximation, where we convert $M_{150\mathrm{c}}$ to $M_{200\mathrm{c}}$ assuming the concentration–mass relation of Diemer & Joyce (2019). We show the probability-weighted halo mass distribution for our NGC 3109 analogues prior to the infall of Antlia or Antlia B in Fig. 2, along with the distribution derived for $M_{200\mathrm{c}}$ assuming that the subhalo masses are approximately $M_{150\mathrm{c}}$. For the range of halo masses (and thus, concentrations) considered here, $M_{200\mathrm{c}}/M_{150\mathrm{c}}$ is typically 0.93–0.96 at $z = 0$, so this correction is modest and allows us to avoid biasing our host selection by including the mass of Antlia in the mass of NGC 3109.

3.3 Summary of analogue selection

With these complexities explained, our analogue selection proceeds as follows. We first identify present-day analogues of NGC 3109 by

Downloaded from https://academic.oup.com/mnras/article/528/1/365/7511121 by guest on 08 December 2024

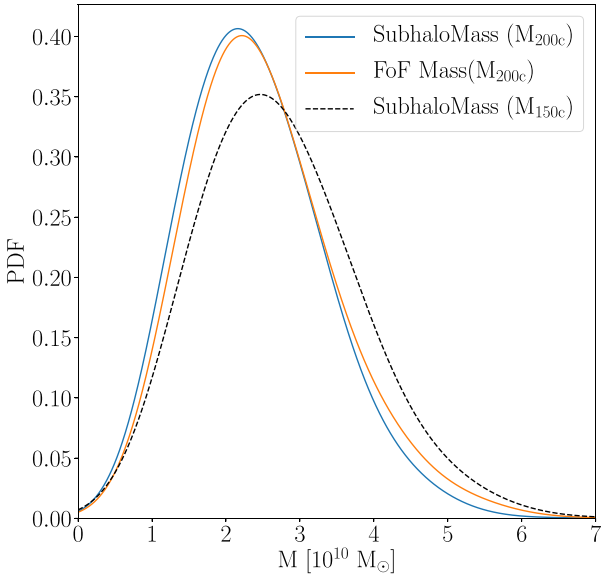

Figure 2. Comparison of the FoF M_{200c} values (orange line) to the SUBLINK subhalo masses (black dashed line) for our NGC 3109 analogues prior to the infall of Antlia or Antlia B. These distributions are weighted by $P(M_{h,\,\mathrm{host},\,i}|M_{*,\,\mathrm{host}})$ for each host i, as given in equation (3). If we assume that the SUBLINK subhalo masses are approximately equal to M_{150c}, we obtain the blue line when we convert them to M_{200c}. This distribution is a good approximation of the FoF M_{200c} distribution, and using the subhalo masses for host selection allows us to avoid including substructure in the host masses, as would be the case if we adopted the FoF masses.

finding all central subhaloes of the FoF groups and assuming their SUBFIND masses are approximately equal to M_{150c}. We convert these to M_{200c} using the concentration–mass relation of Diemer & Joyce (2019), and save all the centrals that have halo masses within the 99.7 per cent credible interval for NGC 3109, given in Table 2. For every subhalo of these centrals identified at present day, we identify each infall event, where the subhalo transitions from being its own central in the FoF catalogues to being a subhalo of the present-day host. We refer to the first infall as being the earliest such event. Note that by requiring subhaloes to be associated with NGC 3109-like hosts at present day, we are excluding splashback haloes which may be beyond the host's virial radius at present day but on a bound orbit. We are also excluding orphaned subhaloes, which do not survive until present day. There are hints that Antlia could be tidally disrupting (Penny et al. 2012) which might support including orphans, but given the limited extent of the disruption likely only $\sim$ 90 per cent of the dark matter halo has been stripped (e.g. Peñarrubia, Navarro & McConnachie 2008), and so we would not expect such a subhalo to be fully disrupted in TNG100. For each infall event, we record the satellite's M_{200c} value from the FoF catalogue of the snapshot prior to infall, when the satellite was its own central, and refer to this value as the infall mass. We note that using the SUBFIND mass and converting it to M_{200c} as we did for the hosts works equally well here, but we prefer to take the M_{200c} directly from the FoF catalogues for the satellites as it avoids assuming a halo concentration. This choice of infall mass does not meaningfully affect our conclusions. Once these infall masses have been recorded, analogues of Antlia and Antlia B are chosen based on the 99.7 per cent credible intervals for each satellite, given in Table 2. Our final sample of Antlia analogues consists of over 5000 subhaloes, while we identify over 20 000 analogue subhaloes for Antlia B.

3.3.1 *A joint sample*

For inclusion in our final sample, we only require that an NGC 3109 analogue have *either* an Antlia analogue or an Antlia B analogue. We formed a separate sample where we required each NGC 3109 analogue to have *both* an Antlia and an Antlia B analogue, but found that the important quantities derived from the simulations (e.g. infall time distributions and orbital trajectories) were consistent between both samples. This 'joint' sample contained $\sim$2500 systems; given that there were 5000 systems with an Antlia analogue and 20 000 systems with an Antlia B analogue when we required only one or the other, we may naively estimate that $\sim$ 50 per cent of systems like NGC 3109 with an Antlia-like satellite also host a satellite like Antlia B, while $\sim$ 12.5 per cent of systems with an Antlia B analogue also host an Antlia analogue. This indicates that, given the presence of Antlia, it is fairly common to find a satellite like Antlia B as well. We additionally find that, even though the infall time distributions of our Antlia and Antlia B analogues are similar (see Section 5.1.1), they rarely fell into their present-day hosts at the same time. Only $\sim$ 5 per cent of systems in the 'joint' sample had their Antlia and Antlia B analogues fall into the NGC 3109 analogue host in the same simulation snapshot, and in only $\sim$ 0.5 per cent of the 'joint' samples were Antlia and Antlia B associated in the snapshot prior to infall. Given that the quantities relevant for our calculation are consistent between the separate and 'joint' samples, and that it is unlikely that Antlia and Antlia B fell in together, we choose to proceed by allowing NGC 3109 analogues to have either an Antlia or an Antlia B analogue to increase our sample size, and we sort the satellites according to whether $P(M_h|M_*)$ (equation 3) is larger for the observed stellar mass of Antlia or Antlia B, given the satellite's halo mass at infall. In cases where an NGC 3109 analogue includes multiple satellites with infall halo masses in our acceptance range (see Table 2), all such satellites are used in our analysis.

3.3.2 *Comparison to TNG50*

We repeated our selection process using data products from the TNG50 (Nelson et al. 2019; Pillepich et al. 2019) simulation, which has a simulation volume roughly $\sim$ 12 per cent of that of TNG100 while evolving an equivalent number of baryonic and dark matter particles, allowing lower mass haloes and galaxies to be resolved in TNG50 than in TNG100. However, given the baryonic particle mass in TNG50 is still 8.4×10^4 $M_\odot$, galaxies with stellar masses less than $\sim 10^7$ $M_\odot$ (like Antlia and Antlia B) are not well resolved in baryons. However, the enhanced resolution in the dark matter component could still be beneficial for our purposes if, for example, it leads to improvements in dynamical accuracy for infalling satellites.

Implementing the same selection procedure outlined above led to a sample of fewer than 300 NGC 3109 analogues with both Antlia and Antlia B analogue satellites. This is roughly 12 per cent as many systems as the $\sim$2500 we found in TNG100, consistent with the difference in the size of the volumes simulated. With fewer than 300 systems, the infall statistics we use as input for our quenching model (e.g. infall time; outlined further in Section 4) show significant Poisson scatter from the small sample size, such that any potential improvement due to the enhanced resolution of TNG50 is counteracted by the much smaller sample size.

In comparing our larger samples, consisting of NGC 3109 analogues with either an Antlia *or* an Antlia B analogue satellite, the samples in TNG50 were large enough to warrant a quantitative comparison to the same samples selected from TNG100. We calculated two of the main infall statistics used as input to our semi-

Downloaded from https://academic.oup.com/mnras/article/528/1/365/7511121 by guest on 08 December 2024

analytic model (the infall times and first pericenter distances; see Section 4) for these samples in both TNG50 and TNG100 and compared them via bootstrap resampling. Assuming Poisson sampling uncertainties, we found the median absolute deviation between the TNG100 distributions and the resampled TNG50 distributions to be $\sim 1.5\sigma$, indicating that there may be slight differences between these quantities in TNG50 and TNG100 but that they are broadly consistent.

For simplicity we compared only the marginal distributions of the satellite infall times and first pericenter distances, but in reality these distributions are covariant with each other, and are likely covariant with other quantities as well (e.g. infall velocity, infall trajectory, etc.). In order to properly sample such a multidimensional distribution, a large sample size is needed to reduce the likelihood of bias in the downstream analysis. As such, we choose to proceed with TNG100 as the quantities relevant for our analysis seem broadly consistent with TNG50, while TNG100 gives us a much larger sample of analogues to use as input for our semi-analytic model.

3.3.3 *Propagating probabilities*

The formalism for calculating the probability that a simulated analogue is representative of an observed satellite has the additional benefit of enabling propagation of these probabilities through further analysis on the simulated analogues. For a quantity X measured from the simulated analogues (e.g. infall time), we define x_i to be the value of X measured for subhalo i. We can derive an improved estimate of the value of X for the observed system by weighting each x_i by the probability that the simulated system is representative of the observed system. Denoting these weights as w_i, we find

$$w_i = P(M_{\mathrm{h,sat},i}|M_{*,\mathrm{sat}})\ P(M_{\mathrm{h,host},i}|M_{*,\mathrm{host}}), \tag{5}$$

where $P(\mathrm{M}_h|\mathrm{M}_*)$ is defined as in equation (4). Estimates can then be made for, e.g. the mean value of X for the observed system as

$$\overline{X} = \frac{\sum_i w_i\, x_i}{\sum_i w_i}. \tag{6}$$

We can incorporate additional data, in particular the projected separation of the satellite and the host and the line-of-sight velocity difference between the two, to further constrain the simulated analogue set. This has historically been done by Monte Carlo rejection sampling, but it can be done more efficiently; in Appendix A, we derive analytic forms for the PDFs of these projected quantities for simulated systems with full 6D information. These probabilities are multiplied into the weights defined in equation (5) to give the final weights for each simulated analogue (equation A6).

4 GAS MASS EVOLUTION

In this section, we describe the semi-analytic framework we develop to assess the relative importance of different quenching mechanisms in terminating star formation in satellite galaxies. The primary mechanisms we assess are starvation (e.g. the cessation of cold gas inflows after infall; Larson et al. 1980; Peng, Maiolino & Cochrane 2015) and RPS (Gunn & Gott 1972). These are the main environmental processes thought to quench star formation of dwarfs after infall (see Cortese, Catinella & Smith 2021 for a review).

In our semi-analytic model, we evolve the H I gas masses of satellites along their orbits in the host potential via a set of coupled ODEs. Once a satellite enters the host halo, with galaxy properties set at infall, we treat the satellite as being starved of gas inflows. In the starvation model, gas is continuously removed from the satellite according to stellar feedback. We treat this gas removal as instantaneously proportional to the star formation rates (SFRs), as inferred from the measured SFHs of the satellites assuming an effective mass-loading factor η for the stellar outflows ($d\mathrm{M}_{\mathrm{gas}}/dt \propto -\eta\, d\mathrm{M}_*/dt$). Unlike other semi-analytic models, we treat RPS as a continuous process, and not as an instantaneous process at pericenter. Because of this, and because of the relatively high mass ratio between the satellite and host haloes, we model the satellite orbits explicitly, including dynamical friction. In this section, we describe how we model the initial conditions and quenching mechanisms and motivate our fiducial parameter choices for our semi-analytic model.

We start in Section 4.1 with a description of the initial conditions for the host and satellite analogues prior to infall. In addition to the satellite stellar masses (which we infer based on the measured SFHs of Antlia and Antlia B) and their infall dark matter halo masses (determined as in Section 3.2), we must specify the dark matter halo concentrations for the orbital integrations, as well as the H I gas surface density profile of the satellite, $\Sigma_{\mathrm{H\,I}}(r)$, and the density profile of the CGM of the host, $\rho_{\mathrm{host}}(R)$, for the RPS calculation. Care in modeling the gas distributions is particularly important for testing RPS as a quenching mechanism.

In Section 4.2, we describe the physics and our specific semi-analytic implementations of starvation and RPS as post-infall quenching mechanisms of satellite star formation. We ignore any quenching process that might begin prior to infall on to the NGC 3109 analogue host. This lack of pre-processing is justified by the simulations of Jahn et al. 2022, who find it unimportant for satellites with stellar masses similar to the Antlias and hosts similar in mass to NGC 3109. We describe our model for each mechanism and motivate our specific parameter choices, and show how we evolve the satellite orbits through the potential of the host with an analytic model for dynamical friction.

Throughout this section, we will focus on our fiducial model while pointing out parts of the model that are uncertain. Results for our fiducial model are presented in Section 5. An exploration of alternate model choices is presented in Section 5.2 and a deeper discussion of model uncertainties is presented in Section 5.3.

4.1 Initial conditions

All integrations of our semi-analytic ODEs are initialized at the lookback time corresponding to the first snapshot in which a satellite was recognized as a subhalo of the host. Important initial conditions include the halo masses of the host and satellite, the stellar mass of the satellite at infall, the CGM density of the host, and the total mass and surface density profile of atomic hydrogen in the satellite.

We take dark matter halo properties (e.g. mass and infall velocity vector) directly from the analogue sample described in Section 3.3. The initial halo mass for the host is taken to be the converted M_{200c} inferred from the *SubhaloMass* column of the simulation catalogues, as discussed in Section 3.2. For the satellite, we set the initial halo mass to be the FoF M_{200c} in the snapshot prior to infall to avoid assuming a halo concentration. We assume the stellar mass of the satellite at infall is fixed according to the measured SFHs of the satellites from Hargis et al. (2020) for Antlia B and Weisz et al. (2011) for Antlia.

We model the density of the host CGM as a singular isothermal sphere ($\rho \propto r^{-2}$), as suggested by simulations (e.g. Fielding et al. 2017; Hafen et al. 2019), with a density normalization of $n = 10^{-3}$ cm^{-3} at 0.1 R_{vir}, following the fiducial high η results from

Downloaded from https://academic.oup.com/mnras/article/528/1/365/7511121 by guest on 08 December 2024

Fielding et al. (2017, see their table 1). We note that the lightest halo considered by Fielding et al. (2017) has a mass of 10^{11} $M_\odot$, with an overdensity criterion of 200 times the mean density of the Universe (i.e. M_{200m}), while our estimated halo mass for NGC 3109 is only 3.87×10^{10} $M_\odot$ based on a density criterion of 200 times the critical density of the Universe (i.e. M_{200c}). From their fig. 7, it is clear the density profile of the CGM, even as a function of r/R_{vir}, evolves with halo mass, especially as the haloes become less massive. Thus this normalization has an uncertainty which we discuss in more detail in Section 5.2.2.

As we integrate the satellite through the host's potential (described in Section 4.2), we do not evolve the masses of the dark matter haloes through the ODE integration, so neither can the host CGM density be evolved. We therefore choose to use the present-day value of the host virial radius to set the density normalization, such that RPS at earlier times will be more effective than in a self-consistently evolved calculation. This has a minimal effect for recent infalls, and we will show that other components of our model (principally, the satellite H I surface density profile) limit the effectiveness of RPS for early infalls, even with this simplification. For our fiducial host halo mass, this corresponds to a cumulative CGM mass within 100 kpc of $\sim 10^9$ $M_\odot$. While generally high η models produce galaxies with clumpier circumgalactic media compared to low η models, we do not attempt to model CGM clumpiness, which would effectively add stochasticity to our gas mass evolutions (Simons et al. 2020; Akins et al. 2021).

For the initial gas masses of the satellites, we use the double-power-law fit of $M_{H\,I}$ to M_* from Bradford et al. (2015), based on measurements of isolated galaxies selected from the NASA Sloan Atlas (Blanton et al. 2011; Geha et al. 2012). Similar fits for samples that are selected via radio or infrared luminosities (e.g. Scoville et al. 2017) generally prefer higher gas masses at lower stellar masses, but are likely biased in this regime due to completeness effects. Typical infall gas masses are $\sim 1.5 \times 10^6$ $M_\odot$ for Antlia B analogues and $\sim 1.7 \times 10^7$ $M_\odot$ for Antlia analogues. We do not include redshift evolution of the H I mass scaling, as theoretical work predicts very weak redshift scaling of the M_*–$M_{H\,I}$ relation out to $2 < z < 3$ (e.g. Popping, Behroozi & Peeples 2015) and there are no observational constraints for such low-mass galaxies at these redshifts. We calculate the stellar masses of the satellites at infall by integrating the SFHs; thus satellites with earlier infalls have lower initial stellar and gas masses. We assume constant SFRs between bins in the SFHs (Weisz et al. 2011; Hargis et al. 2020).

For the satellite H I distributions, we assume an exponential surface density profile $\Sigma_{H\,I}(r) = \Sigma_0 \exp(-r/r_s)$ as is observed over a wide range of $M_{H\,I}$. As galaxies are observed to follow a tight locus in $D_{H\,I}$ (defined as the H I diameter where the surface density equals 1 $M_\odot$ pc^{-2}) and $M_{H\,I}$, we set the initial H I scale radii following this relation, which is given as $\log_{10} D_{H\,I} = 0.506 \log_{10} M_{H\,I} - 3.293$ by Wang et al. (2016), neglecting uncertainties. Typical values of r_s are $\sim$250 pc for Antlia B analogues and $\sim$750 pc for Antlia analogues. The gas scale radius is similar to the stellar half-light radius for Antlia B analogues, while the gas scale radius is about 50 per cent larger than the stellar half-light radius for Antlia analogues. We find typical Σ_0 values of 4.0 $M_\odot$ pc^{-2} for Antlia B analogues and 4.3 $M_\odot$ pc^{-2} for Antlia analogues.

4.2 Quenching models

In this section, we show how we semi-analytically model quenching processes for our analogue NGC 3109 systems. In summary, our quenching model is formulated as a system of ODEs with the following components:

(i) Two-body orbit integration of the satellite and host after first infall, including dynamical friction (Section 4.2.1).
(ii) RPS due to the gaseous halo of the host (Section 4.2.2), which depends on the orbit models in Section 4.2.1.
(iii) Starvation in the satellite due to cessation of gas inflows upon infall and mass-loss due to star-formation-driven outflows (Section 4.2.3).

4.2.1 *Satellite orbits and dynamical friction*

The modeling of RPS in particular requires that we track satellite orbits through the host potential. The time resolution of the IllustrisTNG snapshots is not sufficient to resolve orbits, so we develop the following model to trace orbits to our desired resolution. As noted in Section 3.1, our analysis indicates that Antlia was likely $\sim$ 25 per cent as massive as NGC 3109 at infall. Thus, it is expected that Antlia's infall will induce some reflex motion of the centre of NGC 3109's halo – this invalidates the assumption of a static host potential required for an analytic pericenter estimation, as was employed in Garling et al. (2020). Therefore, we must track the orbital evolution post-infall to determine a reliable pericenter for considering RPS. We take this one step further: by formulating the orbital evolution of the host and satellite as a system of ordinary differential equations (ODE), we can additionally couple the quenching mechanisms directly to the orbit.

We implement the host and satellite system as a system of two rigid, extended bodies (as Gómez et al. 2015 did to study the interaction of the LMC with the MW). We use NFW (Navarro, Frenk & White 1996) density profiles for the dark matter haloes of the galaxies and use the median concentration–mass relation of Diemer & Joyce (2019) as calculated for our adopted Planck 2015 (Planck Collaboration XIII 2016) cosmology to set the scale radii. We set the halo masses of both objects to be constant over the ODE integration and equal to their halo masses at the satellite's first infall. We neglect gravitational forces from the baryonic components of the galaxies, as the stellar-to-halo mass ratios of the satellites are low ($\sim 2 \times 10^{-4}$ for Antlia B and $\sim 7 \times 10^{-4}$ for Antlia).

The system of rigid bodies we have constructed does not experience dynamical friction, which can decrease the pericenter distances of the satellites and thus increase the effectiveness of RPS. It is important that we include dynamical friction because the satellite dark matter haloes are comparable in mass to those of their hosts (see Table 2). We add this effect to the satellite only, using the standard approximation (Chandrasekhar 1943; Binney & Tremaine 2008)

$$\frac{\mathrm{d}\boldsymbol{V}_{\rm sat}}{\mathrm{d}t} = -4\pi G^2 M_{\rm sat} \rho_{\rm host}(R) \ln\Lambda \times \left[\int_0^{|\boldsymbol{V}_{\rm sat}|} v^2 f_{\rm host}(v)\mathrm{d}v\right] \frac{\boldsymbol{V}_{\rm sat}}{|\boldsymbol{V}_{\rm sat}|}^3, \quad (7)$$

where f is the velocity distribution function and Λ is the Coulomb factor. Assuming a Maxwellian velocity distribution, the integral can be approximated as

$$\int_0^{|\boldsymbol{V}_{\rm sat}|} v^2 f_{\rm host}(v)\mathrm{d}v \approx \mathrm{Erf}\,(x) - \frac{2x}{\sqrt{\pi}} \exp\left(-x^2\right). \quad (8)$$

where $x = |\boldsymbol{V}_{\rm sat}|/\sqrt{2\,\sigma^2}$ and σ is the one-dimensional velocity dispersion of the host's dark matter halo. The velocity dispersion

Downloaded from https://academic.oup.com/mnras/article/528/1/365/7511121 by guest on 08 December 2024

can be approximated (e.g. Zentner & Bullock 2003) or calculated by solving the Jeans equation

$$\frac{1}{\rho}\frac{\mathrm{d}(\rho\sigma_r^2)}{\mathrm{d}r} + 2\beta\frac{\sigma_r^2}{r} = -\frac{\mathrm{d}\Phi}{\mathrm{d}r}, \tag{9}$$

where σ_r is the radial velocity dispersion and $\beta(r) = 1 - \sigma_\theta^2(r)/\sigma_r^2(r)$ is a measure of the anisotropy in the velocity distribution. We adopt the solution for constant β and set $\beta = 0.4$ (Łokas & Mamon 2001). For the Coulomb factor, we use the semi-analytic model of Petts, Gualandris & Read (2015) where

$$\begin{aligned} b_{\max} &= \min\left(\rho_{\mathrm{host}}(R) \,/\, \frac{\mathrm{d}\rho_{\mathrm{host}}(R)}{\mathrm{d}r}, R\right), \\ b_{\min} &= \max\left(r_{\mathrm{hm}}, G\,\mathrm{M}_{\mathrm{sat}} \,/\, |\boldsymbol{V}|^2\right), \\ \Lambda &= \begin{cases} \dfrac{b_{\max}}{b_{\min}} \text{ if } b_{\max} > b_{\min} \\ 0, \text{ otherwise} \end{cases}, \end{aligned} \tag{10}$$

where $b_{\max}$ and $b_{\min}$ are the maximum and minimum impact parameters, and r_{hm} is the half-mass radius of the satellite.

4.2.2 Ram pressure stripping

Although RPS was originally formulated in the context of hot gas haloes (e.g. Gunn & Gott 1972; Tonnesen & Bryan 2009; Fillingham et al. 2016; Roberts et al. 2019), evidence is mounting that the cool CGM can contribute significantly to RPS in low-mass hosts (Roediger & Hensler 2005; Simons et al. 2020). RPS proceeds when the ram pressure from the host's gas halo

$$P_{\mathrm{RPS}}(R) = \rho_{\mathrm{CGM}}(R)\,|\boldsymbol{V}_{\mathrm{sat}}|^2 \tag{11}$$

exceeds the maximum gravitational restoring force per unit area of the satellite

$$\begin{aligned} P_{\mathrm{restore}}(r) &= \Sigma_{\mathrm{gas,sat}}(r)\,\frac{G\,M_{\mathrm{sat}}(r)}{r^2} \\ &= \Sigma_{\mathrm{gas,sat}}(r)\,\frac{\mathrm{d}\Phi_{\mathrm{sat}}(r)}{\mathrm{d}r} \end{aligned} \tag{12}$$

for a system with dynamics dominated by a spherical potential, and can be written as

$$P_{\mathrm{RPS}}(R) > P_{\mathrm{restore}}(r). \tag{13}$$

Here, R is the distance from the satellite to the host, r is the distance from the point being considered in the satellite's disc to the satellite's center, G is the gravitational constant, $\Sigma_{\mathrm{gas,\,sat}}(r)$ is the gas surface density of the satellite at r, $M_{\mathrm{sat}}(r)$ is the total mass of the satellite enclosed within radius r, Φ is the gravitational potential of the satellite, $\boldsymbol{V}_{\mathrm{sat}}$ is the velocity vector of the satellite with respect to the host's gaseous halo (called simply $\boldsymbol{V}$ in the prior section), and $\rho_{\mathrm{CGM}}(R)$ is the density of the host's gas halo at R (McCarthy et al. 2008; see also Köppen et al. 2018, which gives an alternate formulation for cases where a stellar disc potential is important). The value of r at which $P_{\mathrm{RPS}} = P_{\mathrm{restore}}$ is called the stripping radius (r_{strip}), and is minimized at pericenter where the host gas halo density and satellite velocity are maximized. For this reason, RPS is often implemented as happening instantly at pericenter or occurring gradually over the relevant pericenter time-scale (e.g. Font et al. 2008). However, not all satellites may experience a pericenter passage by present day. Moreover, most gradual RPS schemes neglect dynamical friction, which is likely to be important for the Antlia analogues, so we adopt a different method for calculating RPS.

To include RPS in our ODE, we require time differentials related to the satellite's orbital parameters in order to evolve the stripping radius and remaining H I mass dynamically. We write the time differential of the RPS pressure as

$$\begin{aligned} \frac{\mathrm{d}\,P_{\mathrm{RPS}}}{\mathrm{d}t} &= \frac{\mathrm{d}\,\rho_{\mathrm{CGM}}(R)}{\mathrm{d}R}\,\frac{\mathrm{d}\,R}{\mathrm{d}t}\,|\boldsymbol{V}_{\mathrm{sat}}|^2 \\ &\quad + 2\,\rho_{\mathrm{CGM}}(R)\,|\boldsymbol{V}_{\mathrm{sat}}|\,\frac{\mathrm{d}\,|\boldsymbol{V}_{\mathrm{sat}}|}{\mathrm{d}t}, \end{aligned} \tag{14}$$

where $\mathrm{d}R/\mathrm{d}t$ in the first term can be written as the scalar product $\boldsymbol{V}_{\mathrm{sat}} \cdot \hat{\boldsymbol{R}}$ with $\hat{\boldsymbol{R}}$ being the unit vector in the direction of the host center. If we assume that the only significant bulk motion of the host's gaseous halo is the reflex motion due to the satellite we can rewrite $\mathrm{d}|\boldsymbol{V}_{\mathrm{sat}}|/\mathrm{d}t$ as $\boldsymbol{a}_{\mathrm{sat}} \cdot \hat{\boldsymbol{V}}_{\mathrm{sat}}$, which gives the component of the acceleration in the direction of the velocity. Substituting these terms, we have

$$\begin{aligned} \frac{\mathrm{d}\,P_{\mathrm{RPS}}}{\mathrm{d}t} &= \frac{\mathrm{d}\,\rho_{\mathrm{CGM}}(R)}{\mathrm{d}R}\,\left(\boldsymbol{V}_{\mathrm{sat}} \cdot \hat{\boldsymbol{R}}\right)\,|\boldsymbol{V}_{\mathrm{sat}}|^2 \\ &\quad + 2\,\rho_{\mathrm{CGM}}(R)\,|\boldsymbol{V}_{\mathrm{sat}}|\,\left(\boldsymbol{a}_{\mathrm{sat}} \cdot \hat{\boldsymbol{V}}_{\mathrm{sat}}\right), \end{aligned} \tag{15}$$

which contains only basic terms related to the orbit and the host gas density profile. With this expression, we can track P_{RPS} explicitly in our ODE. In general, this could be done in a post-processing step after orbit integration, but including the differential for P_{RPS} is useful when using error-controlled, adaptive-timestep ODE integrators.

Additionally, with a differential form for the ram pressure, we can also look for a differential form for the stripping radius. Generally, the stripping radius must be solved numerically (e.g. by root-finding) as the solution of $P_{\mathrm{RPS}} = P_{\mathrm{restore}}$ is rarely analytic. However, the equality $P_{\mathrm{RPS}}(t) = P_{\mathrm{restore}}(r_{\mathrm{strip}})$ which holds at the stripping radius requires that

$$\mathrm{d}P_{\mathrm{RPS}}/\mathrm{d}t = \mathrm{d}P_{\mathrm{restore}}/\mathrm{d}r_{\mathrm{strip}} \times \mathrm{d}r_{\mathrm{strip}}/\mathrm{d}t \tag{16}$$

so that

$$\mathrm{d}r_{\mathrm{strip}}/\mathrm{d}t = \frac{\mathrm{d}P_{\mathrm{RPS}}/\mathrm{d}t}{\mathrm{d}P_{\mathrm{restore}}/\mathrm{d}r_{\mathrm{strip}}}. \tag{17}$$

We have already formulated the time differential for P_{RPS}, so now we need the radial differential for P_{restore} from equation (12), which can be written as

$$\begin{aligned} \frac{\mathrm{d}P_{\mathrm{restore}}}{\mathrm{d}r}(r) &= \frac{\mathrm{d}\,\Sigma_{\mathrm{gas,sat}}}{\mathrm{d}r}(r)\,\frac{\mathrm{d}\Phi_{\mathrm{sat}}}{\mathrm{d}r}(r) \\ &\quad + \Sigma_{\mathrm{gas,sat}}(r)\,\frac{\mathrm{d}^2\Phi_{\mathrm{sat}}(r)}{\mathrm{d}r^2}. \end{aligned} \tag{18}$$

The time differential of r_{strip} is then simply

$$\frac{\mathrm{d}r_{\mathrm{strip}}}{\mathrm{d}t} = \frac{\mathrm{d}P_{\mathrm{RPS}}}{\mathrm{d}t} \,/\, \frac{\mathrm{d}P_{\mathrm{restore}}}{\mathrm{d}r}(r_{\mathrm{strip}}), \tag{19}$$

Thus, we must only compute the stripping radius numerically once to set the initial value, and we can then track its evolution via the differentials, which have components that are analytic for most gas distributions and potentials. We can then write the gas mass differential as

$$\frac{\mathrm{d}\,M_{\mathrm{gas,sat,tot}}}{\mathrm{d}t} = \min\left(0,\ \frac{\mathrm{d}\,M_{\mathrm{gas,sat,enc}}}{\mathrm{d}r_{\mathrm{strip}}}\,\frac{r_{\mathrm{strip}}}{\mathrm{d}t}\right), \tag{20}$$

where $\mathrm{M}_{\mathrm{gas,\,sat,\,enc}}(r)$ is the total gas mass of the satellite enclosed within radius r, and $\min(a, b, c,...)$ is the minimum function, which returns the lesser of its arguments. This differential is always equal to or less than 0 by construction.

4.2.3 Starvation

To define our model for starvation, we begin with our assumptions of the state of the atomic gas in the satellites prior to infall. In isolation, it

Downloaded from https://academic.oup.com/mnras/article/528/1/365/7511121 by guest on 08 December 2024

is typical in semi-analytic models to make gas accretion proportional to the halo mass growth rate (e.g. Benson 2012; Kravtsov & Manwadkar 2022), with the simplest constant of proportionality being the cosmic baryon fraction, Ω_b/Ω_m. In field dwarfs, this accretion rate must outpace star-formation-driven outflows at early times to produce the high $M_{H\,I}/M_*$ ratios that are observed in field dwarfs (generally 1–6 at $M_* = 10^8\,M_\odot$; Papastergis et al. 2012; Popping et al. 2015; Koribalski et al. 2018). Given these high gas fractions, it is understandable that the vast majority of field dwarfs are observed to be actively star forming (e.g. Geha et al. 2012; Dickey et al. 2021).

In starvation, it is assumed that these inflows are shut off after accretion to the host; this is typically explained by the presence of a hot gas halo in the host that intercepts these inflows. Recent simulations suggest that roughly LMC-mass hosts can sustain such a halo (e.g. Jahn et al. 2022), but generally the physical mechanism of starvation is uncertain for such low host masses. With gas accretion shut off, the dwarf can continue to form stars from its gas reservoir. However, this reservoir depletes over time due primarily to star-formation-driven outflows. The gas supply eventually exhausts and star formation is quenched. We thus assume that starvation depends only on time since infall, the star formation rate, and outflows.

We utilize a simple model for starvation, in which there is no net gas accretion to a satellite after infall, and the change in the gas mass is completely specified by

$$\frac{\mathrm{d}M_{\mathrm{gas,sat}}}{\mathrm{d}t} = (R - 1 - \eta(t))\,\frac{\mathrm{d}M_*}{\mathrm{d}t}, \tag{21}$$

where R is known as the recycled fraction and quantifies how much of the gas that goes into forming stars is returned to the ISM, and η is the dimensionless mass-loading factor that relates the gas outflow rate to the SFR $\left(\frac{\mathrm{d}M_*}{\mathrm{d}t}\right)$. We adopt $R = 0.3$ (Portinari, Sommer-Larsen & Tantalo 2004), but it makes little difference given our fiducial mass-loading factors are typically an order of magnitude greater than R. As such, the gas mass-loss rate due to star-formation-driven outflows in our fiducial model ($\eta(t)\,\frac{\mathrm{d}M_*}{\mathrm{d}t}$) is much greater than the rate at which gas mass is locked up in the stars themselves ($(1-R)\,\frac{\mathrm{d}M_*}{\mathrm{d}t} \approx 0.7\,\frac{\mathrm{d}M_*}{\mathrm{d}t}$). To calculate the starvation rate, we utilize the SFH from Hargis et al. (2020) for Antlia B and Weisz et al. (2011) for Antlia.

The key parameter that most influences the importance of starvation is the mass-loading factor, and specifically how it varies as a function of galaxy or halo mass and/or time. For our fiducial model, we adopt the power-law fit of Christensen et al. (2016), which relates the mass-loading factor to the circular velocity at the virial radius as $\eta \propto v_{\mathrm{circ}}^{-2.2}$. This fit is based on hydrodynamical simulations of galaxies with halo virial masses from 3×10^9 to $7 \times 10^{11}\,M_\odot$ using the GASOLINE code (Wadsley, Stadel & Quinn 2004). This halo mass range includes our expectations for both Antlia and Antlia B (see Table 2). Typical mass-loading factors for Antlia and Antlia B with this model are about 6 and 10, respectively. We explore alternate model choices in Section 5.2.1.

5 RESULTS

In this work, we are primarily interested in assessing the relative efficacy of RPS and starvation in quenching satellites of low-mass hosts. This relative efficacy will change depending on the specific choices of the quenching parameters and initial conditions. For a given set of model parameters, the best way to assess the relative efficacy of RPS and starvation is to examine the gas mass evolutions of the set of simulated analogue systems whose final, present-day H I masses are consistent with those observed for the real satellite.

Following this principle, we examine the relative efficacy of RPS and starvation under our fiducial quenching model in Section 5.1. We first present the distributions of infall times and pericenter distances for our full analogue sample to provide insight into the typical properties of the simulated analogue satellites. We then present the mean gas mass evolutions of our Antlia and Antlia B analogues in 1 Gyr bins of infall time under the effects RPS and starvation separately; this allows us to separate the effects of the two quenching mechanisms and illustrate the range of infall times which can reproduce the observed H I masses of the satellites under each.

We then proceed to examine the gas mass evolutions of individual samples under the effects of both RPS and starvation simultaneously to illustrate the variety of evolutionary paths that our satellite analogues take under our fiducial quenching model. In Section 5.2, we examine how our results change under alternate quenching models, and in Section 5.3, we show how observational and theoretical uncertainties affect our conclusions.

5.1 Fiducial model

In this section, we will study the evolution of Antlia B and Antlia analogues from the TNG100 simulations under the fiducial model choices presented in Section 4.1. To facilitate interpretation, we focus on computing expected values and general trends and thus neglect uncertainties in the initial conditions and scaling relations used to compute the gas mass evolution. We discuss some of these sources of uncertainty in Section 5.3 and find that the uncertainties in the absolute quenching time-scales are quite large, typically spanning multiple Gyr. However, our goal is not to robustly estimate the infall times of Antlia and Antlia B using quenching time-scales, but to assess the relative importance of starvation and RPS in depleting the gas reservoirs of these systems, and such relative comparisons are robust to these uncertainties.

Throughout the rest of the paper, weighted distributions utilize the full weights, including halo mass probabilities (Section 3.1) and projected quantity probabilities as defined in equation (A6), while unweighted distributions include only the probabilities of projected quantities as derived in Appendix A, to facilitate comparison to other work and illustrate the difference made by including halo mass probabilities. Generally, including halo mass probabilities makes a 10–20 per cent difference per bin across most distributions. We allow the satellite gas masses to go negative in our ODE integration to facilitate easier comparisons between different infall times, though we mark regions of negative gas masses as unphysical. We begin by discussing the infall time distributions, as these set the relevant quenching time-scales for the satellites.

5.1.1 Satellite infall times

We plot the infall time probability distributions for the Antlia B and Antlia analogues selected from TNG100 in Fig. 3. Distributions weighted only by projected radius and velocity probabilities (Appendix A), as is more typical in the literature, are shown in translucent orange (labelled 'unweighted'), while distributions weighted by host and satellite halo mass probabilities (Section 3.1) in addition to the projected radius and velocity probabilities (Appendix A) are shown in solid blue. The distribution for Antlia B analogues shows a statistically significant peak in the infall time distribution between 1 and 2 Gyr ago, and relatively similar probability from 3 to 7 Gyr ago, with the probability dropping off for earlier infalls. Including

Downloaded from https://academic.oup.com/mnras/article/528/1/365/7511121 by guest on 08 December 2024

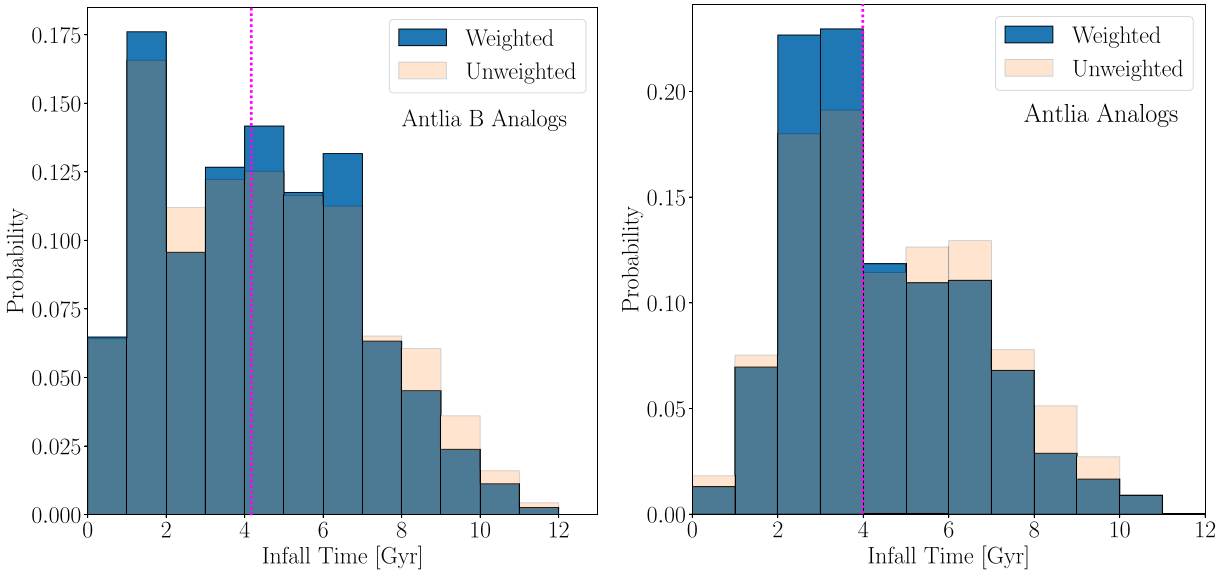

Figure 3. The probability distributions of lookback time at first infall (in Gyr ago) for Antlia B (left) and Antlia (right) analogues selected from TNG100. Weighted distributions are weighted by the host and satellite halo mass probabilities (Section 3.1) in addition to projected quantity probabilities (Appendix A), while unweighted distributions are weighted only by the projected quantity probabilities, as is more typical in the literature. The magenta dashed lines show the weighted median infall times for the analogues, which is about 4 Gyr ago for both satellites.

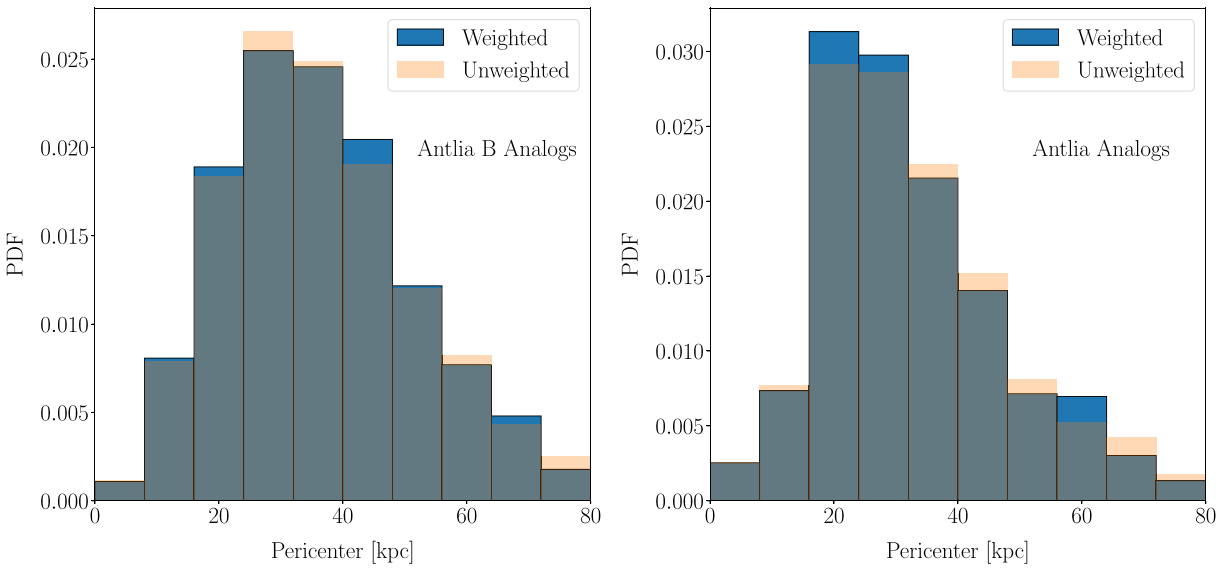

Figure 4. Probability distributions for the host-satellite separation at first pericenter after infall for Antlia B (left) and Antlia (right) analogues selected from TNG100, with weights as in Fig. 3. The distributions are similar, with peaks around ∼30 kpc. About 7 per cent of the analogue satellites experience pericenters ≤10 kpc where tidal stripping may become important (see Section 5.3.3).

the halo mass probabilities in the weights further disfavours earlier infall times. Antlia analogues show a slightly earlier peak in the infall distribution from 2–4 Gyr ago. Similar to Antlia B analogues, the Antlia analogues have fairly flat infall probability from 4 to 7 Gyr ago, with earlier infalls disfavoured. Including the halo mass probabilities in the analysis for the Antlia analogues makes the peak at 2–4 Gyr ago more prominent and disfavours earlier infalls. Overall, the infall time distributions for the Antlia B and Antlia analogues show relatively similar patterns, but it is unlikely they fell into NGC 3109 together; see Section 3.3.1.

5.1.2 *Orbital parameters*

As the pericenter distance of the satellites is important to the effectiveness of RPS, we show the distributions of first pericenters for Antlia B and Antlia analogues in Fig. 4. Only ∼ 7 per cent of analogue satellites experience close pericenters ≤10 kpc for which tidal stripping may be important (see Section 5.3.3). This may partly be due to survivor bias; we require satellites to survive until the present day in TNG100 to be selected, and satellites with small pericenters are more likely to be disrupted. The pericenter

Downloaded from https://academic.oup.com/mnras/article/528/1/365/7511121 by guest on 08 December 2024

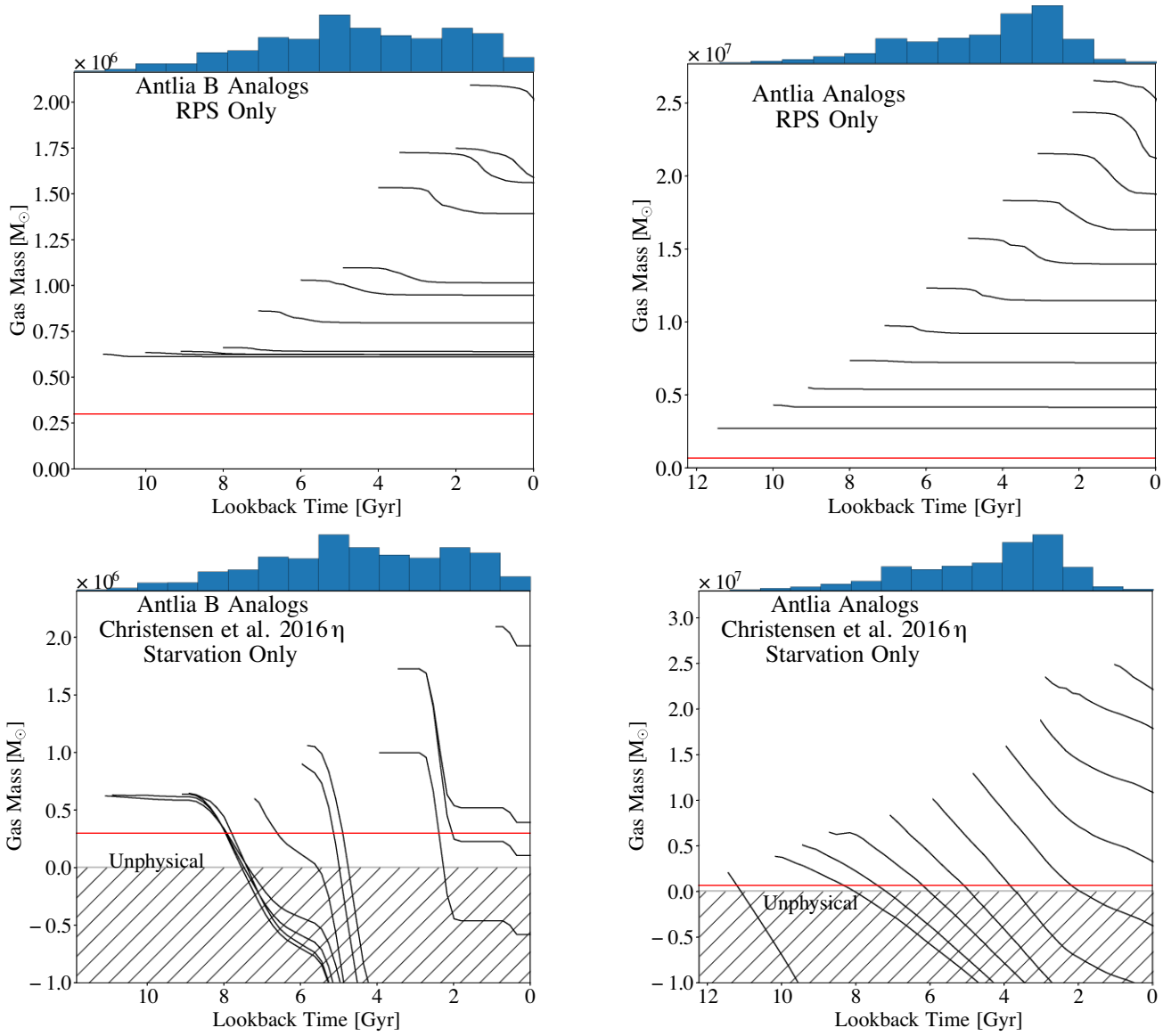

Figure 5. Gas mass evolutions for Antlia B analogues (left column) and Antlia analogues (right column) over the full range of analogue infall times, considering RPS (top row) and starvation (bottom row) separately. The plotted tracks are weighted means across 1 Gyr bins of lookback time, where each sample is weighted by its host and satellite halo mass probabilities (Section 3.1) in addition its projected radius and velocity probabilities (Appendix A). Marginal histograms show the weighted infall time distributions from Fig. 3. Red horizontal lines mark the measured present-day gas masses of Antlia and Antlia B (see Table 1). RPS is ineffective at early times due to our adopted H I mass–size relation producing more compact gas distributions for lower infall gas masses. We find that RPS in our fiducial model produces present-day analogues which are too gas-rich across the entire range of infall times, while starvation can match the observed gas masses for infall times that are likely given the weighted infall time distributions.

distributions reach their peaks at about 20–30 kpc. The means of the distributions are slightly larger than their modes as the distributions are mildly skewed to larger pericenters. Inclusion of halo mass probabilities affects the pericenter distributions minimally.

5.1.3 Mean gas evolution

In Fig. 5, we show the weighted mean gas mass evolutions in 1 Gyr bins of infall time for Antlia B (left column) and Antlia (right column) analogues, considering RPS (top row) and starvation (bottom row) separately. The marginal histograms show the infall time distributions from Fig. 3 for each satellite, while the red horizontal lines mark the present-day observed H I masses from Table 1.

Under our fiducial model, RPS is never effective enough to reproduce the observed H I masses of Antlia and Antlia B on its own. Even for early infall times, which should afford the satellites several pericenters over which to experience RPS, we find that RPS is made ineffective by our assumed H I mass–size relation, which produces more compact gas distributions for lower infall gas masses; such compact distributions are quite resilient to stripping via RPS. Meanwhile, our fiducial starvation model is quite capable of reproducing the observed H I masses for a feasible range of infall times. For Antlia B analogues, infalls in the range of 2–4 Gyr produce comparable H I masses to those observed, and this infall time range is highly probable. For Antlia analogues, infalls in the range of 3–5 Gyr

Downloaded from https://academic.oup.com/mnras/article/528/1/365/7511121 by guest on 08 December 2024

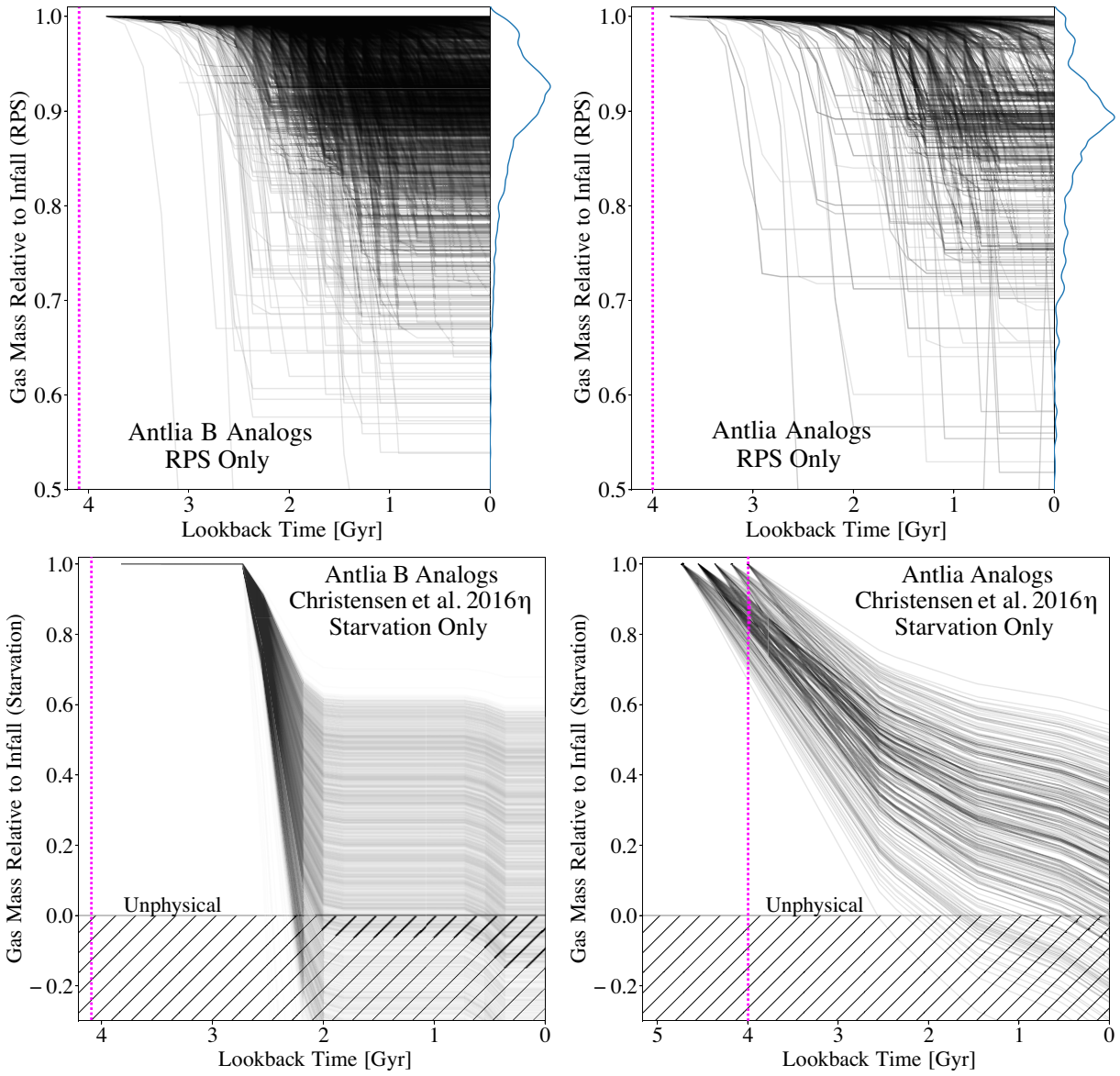

Figure 6. The relative gas mass evolution due to RPS (top row) and starvation (bottom row), calculated as the ratio of the gas mass as a function of time to the infall gas mass, for Antlia B (left column) and Antlia (right column) analogues in the ranges of infall times that give reasonable agreement with the observed H I masses (generally 3–5 Gyr ago). The weighted median infall times for the full samples of Antlia and Antlia B analogues are indicated by vertical magenta dashed lines as in Fig. 3. The majority ($\sim$ 95 per cent) of analogues show less than 20 per cent gas mass-loss due to RPS in this infall time range, while starvation removes the majority of the gas. The variation in the starvation plot is caused by differences in the satellite halo masses at infall.

show good agreement with the observed H I mass, which is again a preferred infall time range based on Fig. 3.

These results indicate that starvation better explains the quenching of the Antlias than RPS. It is also worth looking at how individual systems evolve, and how starvation and RPS act together; we explore this in the next section.

5.1.4 Gas mass evolutions of individual systems

Here, we look at the gas mass evolutions on a per-sample basis in order to understand the variance in the quenching history of the satellite analogues. To simplify this task, we focus on samples in a narrow range of infall times identified in the previous section to give good agreement with the present-day H I mass measurements.

In Fig. 6, we show the gas mass evolutions (as a fraction of infall mass) for individual Antlia and Antlia B samples with infalls roughly 3–5 Gyr ago. We choose this range of infall times because it produces analogues that agree well with the measured present-day H I masses of Antlia and Antlia B when both starvation and RPS are active; these infall times are also highly probable given our simulation sample (Fig. 3). Most satellites in this range of infall time have experienced one to two pericenter passages. We once again separate the effects of starvation and RPS for presentational clarity. The variation in the gas mass evolutions due to starvation is a result of the dependence of the mass-loading factor on the circular velocity of the satellite haloes; since the simulated analogues have different halo masses, they experience slightly different effective mass-loading factors. The variation in gas mass evolutions due to

Downloaded from https://academic.oup.com/mnras/article/528/1/365/7511121 by guest on 08 December 2024

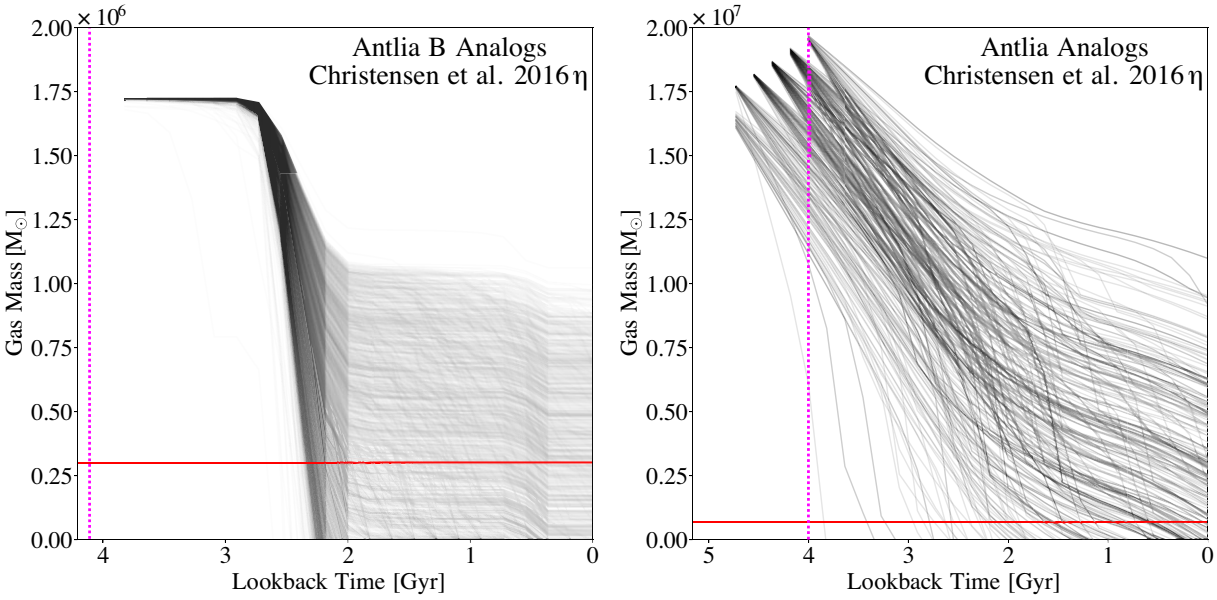

Figure 7. *Left:* The total gas mass evolution including both RPS and starvation for Antlia B analogues with infall times between 3 and 4 Gyr ago. Such an infall time is relatively likely given the weighted distribution of infall times presented in Fig. 3. The weighted median infall time for all Antlia B analogues is indicated by a vertical dashed magenta line as in Fig. 3. The red horizontal line marks the observed H I mass of Antlia B at present day of 2.8×10^5 $M_\odot$ (see Table 1). *Right:* As left, but for Antlia analogues with infall times between 4 and 5 Gyr ago. The red horizontal line marks the observed H I mass of Antlia at present day of 6.8×10^5 $M_\odot$.

RPS is driven primarily by differences in pericenter distances and velocities.

Overall, these plots show that there is a large degree of sample-to-sample variation in the gas mass evolutions. However, it is clear that RPS rarely removes more than 20 per cent of the initial gas mass of satellite analogues that fell into NGC 3109-like hosts between 3 and 5 Gyr ago, while starvation can remove almost an order of magnitude more gas. Typically $\sim$ 12 per cent of the infall gas mass is removed by RPS, while $\sim$ 80 per cent of the infall gas mass is removed by starvation. Only rare, highly radial infalls see greater mass-loss due to RPS, and these infalls are disfavoured due to the observed line-of-sight velocities and 2D projected separations of the satellites from NGC 3109. As such, the most probable orbits for Antlia and Antlia B do not result in significant mass-loss due to RPS.

In reality, both RPS and starvation are likely to act on satellites and a holistic view of quenching should take into account all mechanisms simultaneously. We present absolute gas mass evolutions of individual analogues with both RPS and starvation active in Fig. 7. It is clear that the evolutions are dominated by a similar pattern of mass-loss via starvation, but variations are visible due to the unique signature of RPS.

Due to our wide selection range of satellite halo masses (see Table 2) and our choice of a scaling relation for the mass-loading factor that depends on the halo circular velocity, our satellite analogues can experience quite different strengths of starvation – we find this is actually a larger sample-to-sample variation than that introduced by different RPS strengths.

In summary, the quenching results for individual samples enforce our prior result based on mean evolutions that starvation is significantly more effective than RPS at quenching Antlia and Antlia B analogues in our fiducial model.

5.2 Alternate model parameters

In this section, we consider how varying the key parameters of our quenching models affects the results of the previous section. We identify the primary model parameters as the mass-loading factor (η) for the starvation quenching model and the host CGM density profile ($\rho_{\rm host}(R)$) for the RPS quenching model. For the purpose of presentational clarity, we will discuss other sources of uncertainty stemming from things like initial conditions in Section 5.3.

5.2.1 Mass-loading factors

The strength of starvation as a quenching mechanism is closely tied to the mass-loading factor. To explore how our conclusions depend on this model choice, we examine two alternate models; scaling relations from the FIRE simulations (Muratov et al. 2015) and a constant $\eta = 1$ as is often used in studies of the quenching of MW satellites (Fillingham et al. 2015; Trussler et al. 2020; Jahn et al. 2022).

The scaling relations for mass-loading factors from Muratov et al. (2015) are based on measurements from cosmological FIRE simulations (Hopkins 2012; Hopkins et al. 2014). Of particular interest are two isolated dwarf galaxies in their sample with halo masses of $M_{\rm h} = 2.5$ and 7.8×10^9 $M_\odot$, comparable to the expected halo masses of Antlia B and Antlia, respectively (see Table 2). These simulated galaxies are studied in more detail in Oñorbe et al. (2015). The mass-loading factors reported in those works are larger than some others in the literature (e.g. our fiducial model from Christensen et al. 2016) but some of the difference in the normalization is due to differing outflow definitions. However, Christensen et al. (2016) find that these differing outflow definitions do not resolve the difference in the low-mass slope of the relations; Muratov et al. (2015) find $\eta \propto v_{\rm circ}^{-3.2}$ and Christensen et al. (2016) find $\eta \propto v_{\rm circ}^{-2.2}$. We note that

Downloaded from https://academic.oup.com/mnras/article/528/1/365/7511121 by guest on 08 December 2024

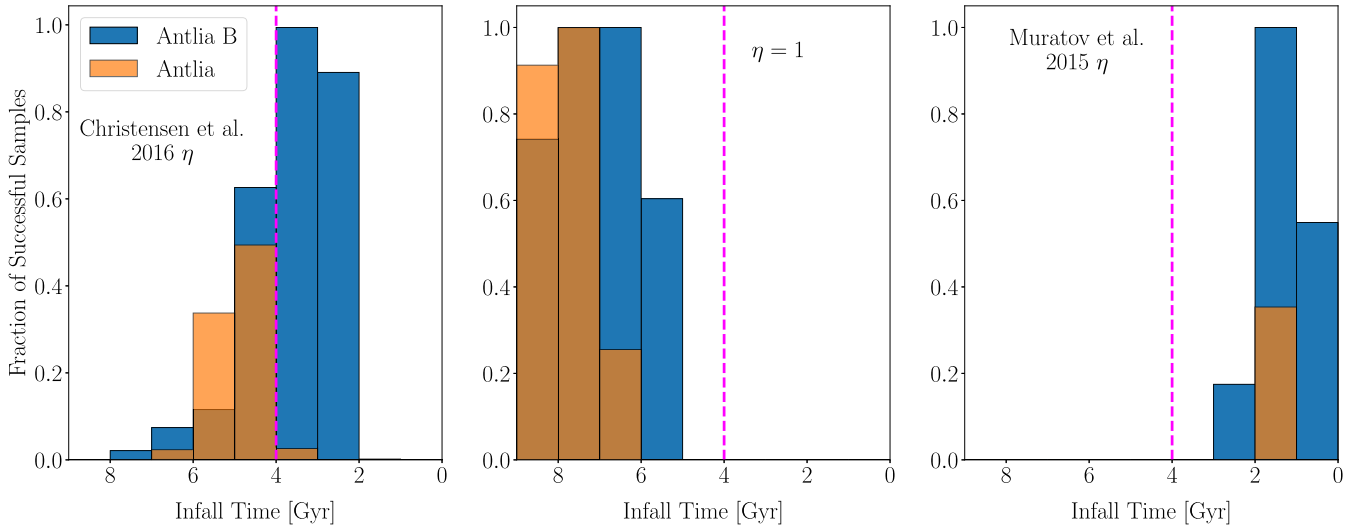

Figure 8. Breakdown of the success of the three mass-loading factors we consider in our starvation model as a function of satellite infall time. A simulated dwarf analogue is counted as a successful sample if the final H I mass at present day is $-2\,M_{\rm obs,H\,I} \leq M_{\rm H\,I} \leq 4\,M_{\rm obs,H\,I}$. The weighted median infall time of Antlia and Antlia B analogues is ∼4 Gyr, indicated by vertical dashed magenta lines. It is clear that the fiducial Christensen et al. (2016) mass-loading factors give the best agreement with the median infall times, while $\eta = 1$ requires earlier infalls to reproduce the observed H I masses, and the Muratov et al. (2015) mass-loading factors require later infalls.

the Muratov et al. (2015) relations may be superseded by Pandya et al. (2021), who use an improved outflow definition and the most recent version of FIRE; they find the same η scaling as Muratov et al. (2015), but a different normalization so that their mass-loading factors are about a factor of two lower. We take the Muratov et al. (2015) values here as representative of the higher mass-loading factors in the literature. Typical mass-loading factors for Antlia and Antlia B with the Muratov et al. (2015) scaling relation are generally $40 < \eta < 60$ and $100 < \eta < 120$, respectively; these are about a factor of ten higher than the Christensen et al. (2016) values.

As expected, the higher mass-loading factors result in much shorter starvation quenching time-scales of about 1–2 Gyr for both satellites such that starvation is even more effective than in the fiducial model. RPS removes almost no gas in comparison; only ∼ 1 per cent of analogues exhibit greater than 5 per cent H I mass-loss due to RPS. If we also increase the initial gas mass by adopting the mean Papastergis et al. (2012) scaling relation between H I mass and stellar mass, then we can obtain similar quenching time-scales to the fiducial model. However, starvation remains much more effective than RPS at quenching these analogues. Coupled with our fiducial Bradford et al. (2015) gas masses (based on a larger sample of low-mass galaxies than Papastergis et al. 2012), the Muratov et al. (2015) mass-loading factors indicate faster quenching and more recent infall times than the infall time distributions shown in Fig. 3 suggest. We show the absolute gas mass evolutions for Antlia and Antlia B analogues with infalls between 1 and 2 Gyr ago using the Muratov et al. (2015) mass-loading factors in Fig. B1.

We next consider a constant $\eta = 1$, corresponding to outflows equal to the instantaneous SFR; such a low mass-loading factor is often utilized in semi-analytic calculations (Fillingham et al. 2015; Jahn et al. 2022; Trussler et al. 2020). As expected, the greatly reduced mass-loading factors translate to much longer quenching time-scales for the satellites, necessitating satellite infalls around 7 to 8 Gyr ago. Analogues with these infall times are able to reproduce the present-day H I masses of Antlia and Antlia B, but such early infalls are relatively rare for the simulated analogues given their infall time distributions (Fig. 3). We additionally note that despite the earlier infall times required by this starvation model allowing for more pericenter passages, there is not a significant increase in the effectiveness of RPS. This is illustrated in the top row of Fig. 5 – satellites with early infall times have lower H I masses at infall than satellites that fall in later, and these lower H I masses imply more centrally concentrated gas distributions which are more resilient to RPS (see the discussion on H I distributions in Section 4.1). We show the absolute gas mass evolutions for Antlia B and Antlia analogues with infall times between 7 and 8 Gyr ago using $\eta = 1$ in Fig. B2.

To summarize the results from our different mass-loading factor models, we show a breakdown of the success of the models as a function of satellite infall time in Fig. 8. A simulated analogue is a 'successful' sample if its final H I mass at present day is $-2\,\mathrm{M_{obs,H\,I}} \leq \mathrm{M_{H\,I}} \leq 4\,\mathrm{M_{obs,H\,I}}$, with this range chosen to highlight the differences between the models. It is clear from this comparison that the fiducial Christensen et al. (2016) mass-loading factors are completely consistent with the weighted median infall times of Antlia and Antlia B, which are both ∼4 Gyr (see Fig. 3). With $\eta = 1$, quenching is much slower, necessitating considerably earlier infalls, which are rare for our simulated samples. Conversely, the high Muratov et al. (2015) mass-loading factors require quite late infall times, generally within the last 2 Gyr. This demonstrates the importance of including realistic mass-loading factors when considering the quenching time-scales of low-mass dwarfs post-infall.

5.2.2 *Alternate host CGM models*

As the ram pressure experienced by the satellite is linearly related to the host CGM density (equation 11), our conclusions about the efficacy of RPS depend directly on our assumptions about the host CGM. Though our fiducial singular isothermal sphere density model is well supported by simulations (e.g. Fielding et al. 2017; Hafen et al. 2019), the normalization (and thus, the total mass in the CGM) is significantly more uncertain, especially for galaxies as low-mass as NGC 3109. Under our fiducial normalization, the total mass in the

Downloaded from https://academic.oup.com/mnras/article/528/1/365/7511121 by guest on 08 December 2024

CGM of NGC 3109 within 100 kpc of its center is $\sim 10^9$ M$_\odot$; here, we examine changes in the effectiveness of RPS when increasing the total CGM mass of our hosts.

Under our fiducial host CGM model, Antlia and Antlia B analogues with infalls around 4 Gyr ago lose $\sim$ 10 per cent of their infall H I mass due to RPS (see the left column of Fig. 6). If we increase the host CGM mass by a factor of two, to $\sim 2 \times 10^9$ M$_\odot$, we see an additional $\sim$ 4 per cent mass-loss due to RPS, for an average H I mass-loss due to RPS of $\sim$ 14 per cent of the infall H I mass. Analogues with earlier infall times still do not experience significant mass-loss due to RPS because their H I distributions are more compact at infall (see the top row of Fig. 5). If we increase the host CGM mass by a factor of four, to $\sim 4 \times 10^9$ M$_\odot$, we see a greater change in the H I mass-loss, which becomes $\sim$ 22 per cent of the infall H I mass. The CGM mass must be $\sim 2.5 \times 10^{10}$ M$_\odot$ before we reach 50 per cent mass-loss due to RPS, a factor of 25 greater than our fiducial value and nearly equal to our estimated halo mass for NGC 3109 of 3.87×10^{10} M$_\odot$ (see Table 2).

Even with a significantly increased CGM mass, we do not find it plausible that Antlia and Antlia B were quenched via RPS. Even with a host CGM four times more massive than in our fiducial model, Antlia and Antlia B analogues with infalls around 4 Gyr ago are too H I-rich at present day, having 5–10 times more mass in H I than is measured for the real satellites. Analogues with earlier infall times are no better; they experience less mass-loss due to RPS because they have more compact H I distributions at infall. This reinforces our conclusion that starvation is necessary for the quenching of Antlia and Antlia B and shows that our results are robust to uncertainties in the host CGM normalization.

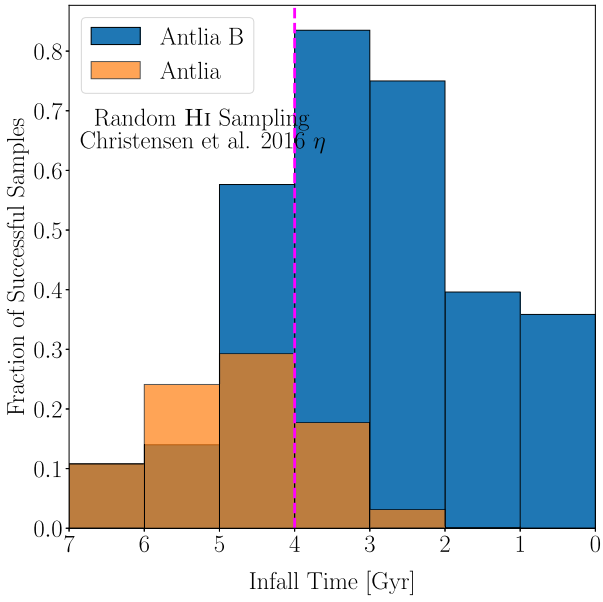

Figure 9. The fraction of analogue satellites in 1 Gyr bins of infall time with final H I masses at present day between $-2\,M_{\rm obs,H\,I} \leq M_{\rm H\,I} \leq 4\,M_{\rm obs,H\,I}$ when randomly sampling the H I mass of the satellites at infall according to the empirical scatter (Bradford et al. 2015). This is analogueous to the left panel of Fig. 8, but includes the empirical uncertainty on the H I masses at infall. In comparison, including uncertainty on the infall H I masses broadens the distribution of plausible infall times, but does not meaningfully change our conclusions.

5.3 Model uncertainties

Having examined the dependence of our results on the key model parameters, we now move on to discuss other sources of uncertainty in our analysis. These relate in particular to initial conditions (e.g. the initial H I masses of the satellites at infall) and observational quantities of the NGC 3109 system (e.g. the assumed SFHs of the satellites).

5.3.1 Initial H I *mass*

Our experimental set-up with a fixed, empirical SFH is quite sensitive to the choice of satellite H I mass at infall. We demonstrated this in Section 5.2.1, where we computed gas mass evolutions under the Muratov et al. (2015) mass-loading factors with two different models for satellite H I masses at infall. For these high mass-loading factors, the change in infall H I masses led to satellite quenching times that were a factor of $\sim$2 different. However, we have thusfar neglected scatter in the empirical relation we assume for our fiducial infall H I masses (Bradford et al. 2015). Given the dependence of the quenching behaviour on the initial H I mass, it is reasonable to question what effect including the empirical scatter in our model has on our conclusions.

With the simplicity of the quenching models, we can reason about the effects of including uncertainty on the initial H I. Under our fiducial model, namely the double-power-law fit of $M_{\rm H\,I}$ to M_* from Bradford et al. (2015), the initial H I masses of Antlia and Antlia B analogues are typically $\sim$25 and $\sim$5 times greater than their present day measured H I masses, respectively. If we model the intrinsic scatter as lognormal, as indicated in the literature (e.g. Papastergis et al. 2012; Bradford et al. 2015; Scoville et al. 2017), it is clear that the spread in the initial H I masses will be comparable to or greater in magnitude than the target final H I mass. For instance, if the expected initial H I mass at a given infall time for an Antlia B analogue is 1.5×10^6 M$_\odot$, then a 0.2 dex lognormal scatter results in a 1σ range of roughly $1.5^{+0.8}_{-0.5} \times 10^6$ M$_\odot$ at fixed infall time, while the present-day observational value is 3×10^5 M$_\odot$.

We can see how this uncertainty affects our analogue samples in Fig. 9, which is analogueous to the left panel of Fig. 8, but where we have randomly sampled the initial H I masses of the satellites at infall according to a lognormal distribution with 0.2 dex of scatter as discussed above. Including this uncertainty allows for a broader range of analogue infall times to produce final H I masses that are comparable to the observed values for the satellites. This effect is stronger for more recent infall times, as more recent infalls have higher mean H I masses at infall under our fiducial model, leading to larger scatter under the lognormal distribution. Including this uncertainty does not lead to any significant increase in the average effect of RPS; it remains relatively ineffective at removing gas from our satellite analogues in the presence of this uncertainty. We additionally see that when accounting for this uncertainty, the mean infall times of our simulated analogues still agree well with the distribution of successful samples.

In addition to this large intrinsic scatter, there is also some disagreement in the literature about the low-mass slope of the M_*–$M_{\rm H\,I}$ relation. If we adopt instead the power-law fit of $M_{\rm H\,I}$ to M_* from Papastergis et al. (2012), we find expected initial H I masses for Antlia and Antlia B that are factors of 2.5 and 7.5 higher than our fiducial values utilizing the relation from Bradford et al. (2015). As we have shown that the simulated present-day H I masses scale almost linearly with the initial H I masses, adopting the Papastergis et al. (2012) relation would translate to quenching time-scales a few

Downloaded from https://academic.oup.com/mnras/article/528/1/365/7511121 by guest on 08 December 2024

Gyr longer than we obtain with the fiducial H I masses based on the results of Bradford et al. (2015). The larger initial H I masses result in more extended satellite H I distributions under our surface density model (Section 4.1) such that RPS is slightly more effective, stripping on average $\sim 15-20$ per cent of the infall H I masses of Antlia and Antlia B analogues compared to an average of ~ 10 per cent under our fiducial model. However, significantly more gas needs to be removed to reproduce the present-day satellite H I masses, and RPS cannot remove all of this gas on its own – the majority of analogues end up with present-day H I masses that are at least 5–10 times higher than the observed values under the effects of RPS alone.

As the large uncertainty in the initial H I mass propagates to the final present-day H I mass, the quenching time-scales quoted throughout the paper should be regarded as expectation values with relatively large uncertainties ($\sim$1 Gyr). However, our conclusion that starvation is more effective at quenching Antlia and Antlia B analogues is robust in the presence of this uncertainty due to the weak scaling of RPS mass-loss with the initial H I mass for our adopted gas surface density model.

5.3.2 SFHs and stellar masses

In this section, we consider the effects of the uncertainty in the SFHs of the two satellites on our inferences about the relative efficacy of quenching mechanisms. For SFHs derived from resolved stellar photometry, such as we use here, there is generally an anticorrelation between adjacent time bins in the absolute SFH (i.e. the total amount of stellar mass formed in a time bin) because if the SFR is overestimated in bin i, it is typically underestimated in bin $i+1$ due to the similarities in the color-magnitude diagrams (Weisz et al. 2011; Dolphin 2013). However, this trait is removed by constructing a cumulative SFH (i.e. the sum of all stellar mass formed up to and including bin i) and normalizing it to the final integrated stellar mass. In a cumulative SFH, the uncertainties in adjacent time bins are uncorrelated. We use these cumulative SFHs for our analysis and normalize them to the stellar masses in Table 1. In our simple starvation model, neglecting time-evolution of the mass-loading factor η, the present-day gas mass considering only starvation is simply $M_{\mathrm{H\,I},z=0} = M_{\mathrm{H\,I,infall}} + (R-1-\eta)\,\Delta M_*$ where $\Delta M_* = M_{*,z=0} - M_{*,\mathrm{infall}}$ is the total stellar mass formed between infall and the present day. Since η is at least an order of magnitude greater than R for the dwarf masses considered here, the scatter in the present-day H I mass will approximately scale with η and the uncertainty in $M_{*,z=0}$.

As the uncertainties in the present-day stellar masses are of the same order as the present-day H I masses, and the time-averaged η for Antlia and Antlia B are about 6 and 10, respectively, the stellar mass uncertainties introduce a large uncertainty on the present-day H I mass. This uncertainty is subdominant to the uncertainty in the initial H I mass for Antlia analogues, but is about a factor of 2–4 greater than the uncertainty in the initial H I mass for Antlia B analogues due to the larger mass-loading factors of Antlia B analogues. It should also be clear that since the initial H I masses are based on the stellar masses, uncertainty in the stellar masses will also increase the scatter in the initial H I masses. We do not explore this correlation further, as we have demonstrated that the uncertainties in the initial H I masses and SFHs introduce significant errors into the present-day H I mass estimates at fixed infall time. We reiterate that, given these large uncertainties, the absolute quenching time-scales derived in Section 5.1 are largely uncertain, but conclusions about the relative efficacy of starvation and RPS remain robust.

5.3.3 Tidal stripping

In our fiducial model, we neglect tidal stripping in order to simplify the orbital evolution. However, it is worth considering whether tidal stripping affects the gas reservoirs of our analogue satellites. If the tidal radius is at any point smaller than the historical minimum of the RPS stripping radius, then tidal stripping may remove additional gas from the satellite. Adopting the definition of tidal radius from Peñarrubia et al. (2008) of $\langle\rho_{\mathrm{sat}}(r_t)\rangle = 3\,\langle\rho_{\mathrm{host}}(R)\rangle$ where $\langle\rho_{\mathrm{sat}}(r_t)\rangle$ is the mean dark matter density of the satellite inside the tidal radius and $\langle\rho_{\mathrm{host}}(R)\rangle$ is the mean dark matter density of the host inside R, which is the distance between the host and satellite centers. We observe median pericenters of $\sim$35 and $\sim$45 kpc for Antlia and Antlia B analogues, respectively, and find tidal stripping radii at these pericenters greater than 10 kpc, at least twice as large as the RPS stripping radius. The tidal radius is similar to the RPS stripping radius for pericenters around 10 kpc, with a typical value of $\sim$3 kpc for Antlia analogues and $\sim$1 kpc for Antlia B analogues, though we have few analogue samples with such small pericenters. For pericenters closer than 10 kpc, tidal stripping can remove gas if the velocity of the satellite is low enough, but only ~ 7 per cent of the analogue satellites have such close pericenters (Fig. 4). It therefore seems unlikely that tidal stripping is a significant quenching mechanism for hosts of NGC 3109's mass.

Given these calculations, we can comment briefly on the observation of elongation of the stellar component of Antlia presented in Penny et al. (2012), which they suggested may be due to tidal disruption. Given Antlia's stellar effective radius of $\sim$500 pc and assuming that the full extent of the stellar population is $\sim$1 kpc, we see that the tidal stripping radius is beyond the stellar radius for even very close pericenters ($<$10 kpc), due in large part to the fact that our expected halo mass for Antlia is roughly a quarter that of NGC 3109 and so is larger than assumed in their work. As such, for our simulation sample and adopted halo mass ranges, tidal stripping of Antlia's stars seems quite unlikely. However, it is still possible, as they argue, that an increase in the internal binding energy of the satellite may lead to partial dissolution. A full exploration of the possible tidal disruption of Antlia's stellar population is beyond the scope of this work.

We note that the above calculations assume the satellite dwarfs inhabit cuspy dark matter haloes that can be approximated by NFW density profiles. It is well established that dwarf galaxies in nature exhibit a variety of density profiles, including so-called cored profiles that have lower central densities than are predicted from dark-matter-only simulations for haloes of equivalent mass (e.g. Oh et al. 2015). If Antlia or Antlia B have dark matter cores, then tidal stripping would be more effective (e.g. Errani et al. 2023) and could play a more substantial role in star formation quenching if either dwarf has had a close pericenter passage, as discussed above. Unfortunately, there are no current observational constraints on the density profiles of Antlia or Antlia B that we can use to inform this analysis.

6 CONCLUSION

In order to study the quenching mechanisms relevant for satellites of low-mass hosts, we have selected systems analogueous to NGC 3109, which hosts two satellites, Antlia and Antlia B, both of which have well-measured H I masses and SFHs (see Table 1 for observational properties and Table 2 for halo mass estimates). Analogues are selected from the cosmological TNG100 simulation with hydrodynamics (Nelson et al. 2018; Naiman et al. 2018; Springel et al. 2018; Pillepich et al. 2018b; Marinacci et al. 2018). We

Downloaded from https://academic.oup.com/mnras/article/528/1/365/7511121 by guest on 08 December 2024

derive halo mass probability distributions for the observed galaxies, allowing us to select a larger sample of analogues and propagate the probability that they represent the observed system through our analysis. We additionally derive probability distributions for the projected separations and line-of-sight velocities of the simulated systems and utilize the observational data to further constrain our analogue sample.

With simulated analogues in hand, we construct an observationally constrained semi-analytic model to study the evolution of the gas masses of the satellites after infall. We implement gas mass-loss due RPS and starvation (i.e. cessation of cold gas inflows) in the semi-analytic model, and examine tidal stripping in post-processing. Because we estimate that Antlia was about 25 per cent as massive as NGC 3109 at first infall, we resimulate the orbits of all systems, including a model for dynamical friction, from first infall to the present day to properly model RPS. Rather than self-consistently evolving the star formation, we fix the SFHs of the satellites to the observed values when computing the mass-loss due to starvation.

For our fiducial quenching models, we find that starvation is much more effective than RPS. In particular, ~ 95 per cent of analogue satellites have less than 20 per cent of their initial H I removed by RPS, which is insufficient to produce the present day observed H I masses unless the infall gas masses of the satellites were an order of magnitude lower than our fiducial values. Only for rare (< 1 per cent of samples), highly radial orbits is RPS able to strip a significant fraction of gas. We additionally show that the tidal stripping radius is almost always larger than the RPS stripping radius in our model, such that tidal stripping is incapable of removing a significant amount of gas under the vast majority of likely satellite orbits. In contrast, we find starvation to be highly effective, producing reasonable agreement with the observed present-day gas masses for infall times between 3 and 4 Gyr ago for Antlia and 4–5 Gyr ago for Antlia B, squarely in the middle of the infall time probability distributions indicated in the TNG100 simulations. While absolute quenching time-scales are difficult to constrain due to uncertainties in the initial conditions for our semi-analytic model, it is clear from our results that starvation is the primary quenching mechanism for Antlia and Antlia B under our fiducial model choices.

To survey the range of model parameters supported by the literature, we examine two alternate mass-loading factors, including a constant $\eta = 1$ and the relation between η and M_* given in Muratov et al. (2015), with the former being lower than the fiducial values from Christensen et al. (2016) and the latter being higher. For the Muratov et al. (2015) relation, we find much shorter quenching time-scales as expected, with starvation being perhaps *too* effective, as the quenching time-scales for starvation with the Muratov et al. (2015) model are as short as 1–2 Gyr. For $\eta = 1$, we find much longer quenching time-scales that imply first infalls around 7–8 Gyr ago, which are unlikely for our sample; importantly, we still find that starvation is the main mechanism that removes gas from the dwarfs, even with such a low mass-loading factor.

Our results suggest that starvation is significantly more effective than RPS at removing gas from the satellites of such low-mass hosts. This is in contrast to some recent work with hydrodynamic simulations (e.g. Jahn et al. 2022) that suggests RPS is the dominant quenching mechanism at this mass scale. However, it is difficult to differentiate between starvation and RPS in hydrodynamic simulations because energetic stellar feedback may 'loosen' the gas of the dwarf satellites, allowing it to be more easily stripped by RPS. Such 'weak' RPS, which primarily only removes such loosened gas, could be differentiated from 'strong' RPS that directly strips the dense interstellar media of the dwarf satellites (as implemented in our model) by testing whether gas particles ejected from the dwarf galaxy were recently exposed to stellar feedback (e.g. a supernova).

Given these simulation results, we find it likely that 'weak' RPS may explain starvation in low-mass systems by both intercepting pristine gas inflows and preventing satellites from re-accreting metal-enriched outflows. Such a scenario does not require 'strong' RPS to directly remove cold, dense H I from the discs of accreted satellites, which we have shown to be ineffective at these mass scales. This scenario does, however, require that low-mass galaxies have circumgalactic media or bulk outflows that are capable of causing this 'weak' RPS as is indicated by recent work at mass scales slightly above that of NGC 3109 (e.g. Bordoloi et al. 2014; Johnson et al. 2017; Fielding et al. 2017; Hafen et al. 2019; Pandya et al. 2021; Jahn et al. 2022). Given these results, our work with the satellites of the NGC 3109 system suggests that outflows play a major dual role in the evolution of satellites: outflows from low-mass hosts cause 'starvation' by preventing gas from being accreted on to dwarf satellites, and outflows from dwarf satellites dramatically shorten the time-scale for quenching once satellites are disconnected from their gas supply. Extending observational and theoretical studies of star-formation-driven outflows and galactic CGM to lower galaxy masses will shed further light on this subject.

ACKNOWLEDGEMENTS

We would like to thank Stephanie Tonnesen for helpful discussions regarding RPS. We also thank Carton Zeng for helpful comments. CTG and AHGP are primarily supported by the National Science Foundation (NSF) grant no. AST-1813628, and additionally supported by NSF grant no. AST-1615838. KS acknowledges support from the Natural Sciences and Engineering Research Council of Canada (NSERC). DJS acknowledges support from NSF grants AST-1821967 and 1813708. Research by DC is supported by NSF grant AST-1814208. JLC acknowledges support from *HST* grant HST-GO-15228 and NSF grant AST-1816196.

This research has made use of the NASA/IPAC Extragalactic Database (NED), which is operated by the Jet Propulsion Laboratory, California Institute of Technology, under contract with the National Aeronautics and Space Administration. This research has made use of NASA's Astrophysics Data System.

DATA AVAILABILITY

The IllustrisTNG data products used in this work are publicly available. Output from our semi-analytic model is proprietary but may be shared on reasonable request to the corresponding author.

REFERENCES

Akins H. B., Christensen C. R., Brooks A. M., Munshi F., Applebaum E., Engelhardt A., Chamberland L., 2021, ApJ, 909, 139
Applebaum E., Brooks A. M., Christensen C. R., Munshi F., Quinn T. R., Shen S., Tremmel M., 2021, ApJ, 906, 96
Barnes D. G., de Blok W. J. G., 2001, AJ, 122, 825
Baxter D. C., Cooper M. C., Fillingham S. P., 2021, MNRAS, 503, 1636
Behroozi P. S., Wechsler R. H., Conroy C., 2013, ApJ, 770, 57
Behroozi P., Wechsler R. H., Hearin A. P., Conroy C., 2019, MNRAS, 488, 3143
Benson A. J., 2012, New Astron., 17, 175

Downloaded from https://academic.oup.com/mnras/article/528/1/365/7511121 by guest on 08 December 2024

Benson A. J., Lacey C. G., Baugh C. M., Cole S., Frenk C. S., 2002, MNRAS, 333, 156
Besla G. et al., 2018, MNRAS, 480, 3376
Binney J., Tremaine S., 2008, Galactic Dynamics, 2nd edn. Princeton Univ. Press, Princeton http://adsabs.harvard.edu/abs/2008gady.book.....B
Birnboim Y., Dekel A., 2003, MNRAS, 345, 349
Blais-Ouellette S., Amram P., Carignan C., 2001, AJ, 121, 1952
Blanton M. R., Kazin E., Muna D., Weaver B. A., Price-Whelan A., 2011, AJ, 142, 31
Bordoloi R. et al., 2014, ApJ, 796, 136
Bradford J. D., Geha M. C., Blanton M. R., 2015, ApJ, 809, 146
Brown T. M. et al., 2014, ApJ, 796, 91
Buck T., Macciò A. V., Dutton A. A., Obreja A., Frings J., 2019, MNRAS, 483, 1314
Bullock J. S., Kravtsov A. V., Weinberg D. H., 2000, ApJ, 539, 517
Butcher H., Oemler A., Jr, 1984, ApJ, 285, 426
Campbell D., van den Bosch F. C., Padmanabhan N., Mao Y.-Y., Zentner A. R., Lange J. U., Jiang F., Villarreal A., 2018, MNRAS, 477, 359
Cardelli J. A., Clayton G. C., Mathis J. S., 1989, ApJ, 345, 245
Carlin J. L. et al., 2016, ApJ, 828, L5
Carlin J. L. et al., 2019, ApJ, 886, 109
Carlin J. L. et al., 2021, ApJ, 909, 211
Carlsten S. G., Greene J. E., Greco J. P., Beaton R. L., Kado-Fong E., 2021, ApJ, 922, 267
Carlsten S. G., Greene J. E., Beaton R. L., Greco J. P., 2022, ApJ, 927, 44
Chambers K. C. et al., 2016, preprint (arXiv:1612.05560)
Chandrasekhar S., 1943, ApJ, 97, 255
Christensen C. R., Davé R., Governato F., Pontzen A., Brooks A., Munshi F., Quinn T., Wadsley J., 2016, ApJ, 824, 57
Cook D. O. et al., 2014, MNRAS, 445, 881
Cooper M. C. et al., 2006, MNRAS, 370, 198
Cortese L., Catinella B., Smith R., 2021, PASA, 38, e035
Dalcanton J. J. et al., 2009, ApJS, 183, 67
Davé R., Rafieferantsoa M. H., Thompson R. J., 2017, MNRAS, 471, 1671
Davies L. J. M. et al., 2019, MNRAS, 483, 5444
Davis A. B. et al., 2021, MNRAS, 500, 3854
Dickey C. M. et al., 2021, ApJ, 915, 53
Diemer B., Joyce M., 2019, ApJ, 871, 168
Digby R. et al., 2019, MNRAS, 485, 5423
Di Matteo T., Springel V., Hernquist L., 2005, Nature, 433, 604
Dolphin A. E., 2013, ApJ, 775, 76
Dooley G. A., Peter A. H. G., Yang T., Willman B., Griffen B. F., Frebel A., 2017, MNRAS, 471, 4894
Dressler A., 1980, ApJ, 236, 351
Driver S. P. et al., 2011, MNRAS, 413, 971
Eisenstein D. J., Hu W., 1999, ApJ, 511, 5
Emerick A., Low M.-M. M., Grcevich J., Gatto A., 2016, ApJ, 826, 148
Errani R., Navarro J. F., Peñarrubia J., Famaey B., Ibata R., 2023, MNRAS, 519, 384
Fielding D., Quataert E., McCourt M., Thompson T. A., 2017, MNRAS, 466, 3810
Fillingham S. P., Cooper M. C., Wheeler C., Garrison-Kimmel S., Boylan-Kolchin M., Bullock J. S., 2015, MNRAS, 454, 2039
Fillingham S. P., Cooper M. C., Pace A. B., Boylan-Kolchin M., Bullock J. S., Garrison-Kimmel S., Wheeler C., 2016, MNRAS, 463, 1916
Fillingham S. P. et al., 2019, preprint (arXiv:1906.04180)
Font A. S. et al., 2008, MNRAS, 389, 1619
García-Benito R., Delgado R. M. G., Pérez E., Fernandes R. C., Sánchez S. F., de Amorim A. L., 2019, A&A, 621, A120
Garling C. T., Peter A. H. G., Kochanek C. S., Sand D. J., Crnojević D., 2020, MNRAS, 492, 1713
Garrison-Kimmel S. et al., 2019, MNRAS, 489, 4574
Gatto A., Fraternali F., Read J. I., Marinacci F., Lux H., Walch S., 2013, MNRAS, 433, 2749
Geha M., Blanton M. R., Yan R., Tinker J. L., 2012, ApJ, 757, 85
Geha M. et al., 2017, ApJ, 847, 4
Genel S., Vogelsberger M., Nelson D., Sijacki D., Springel V., Hernquist L., 2013, MNRAS, 435, 1426
Gómez F. A., Besla G., Carpintero D. D., Villalobos Á., O'Shea B. W., Bell E. F., 2015, ApJ, 802, 128
Grcevich J., Putman M. E., 2009, ApJ, 696, 385
Gunn J. E., Gott J. R. III, 1972, ApJ, 176, 1
Hafen Z. et al., 2019, MNRAS, 488, 1248
Haines C. P., Gargiulo A., La Barbera F., Mercurio A., Merluzzi P., Busarello G., 2007, MNRAS, 381, 7
Hargis J. R. et al., 2020, ApJ, 888, 31
Hogg D. W. et al., 2003, ApJ, 585, L5
Hopkins P. F., 2012, MNRAS, 428, 2840
Hopkins P. F., Kereš D., Oñorbe J., Faucher-Giguère C.-A., Quataert E., Murray N., Bullock J. S., 2014, MNRAS, 445, 581
Jahn E. D., Sales L. V., Wetzel A., Boylan-Kolchin M., Chan T. K., El-Badry K., Lazar A., Bullock J. S., 2019, MNRAS, 489, 5348
Jahn E. D., Sales L. V., Wetzel A., Samuel J., El-Badry K., Boylan-Kolchin M., Bullock J. S., 2022, MNRAS, 513, 2673
Jarrett T. H., Chester T., Cutri R., Schneider S. E., Huchra J. P., 2003, AJ, 125, 525
Jethwa P., Erkal D., Belokurov V., 2018, MNRAS, 473, 2060
Johnson S. D., Chen H.-W., Mulchaey J. S., Schaye J., Straka L. A., 2017, ApJ, 850, L10
Karunakaran A. et al., 2021, ApJ, 916, L19
Kauffmann G., White S. D. M., Heckman T. M., Ménard B., Brinchmann J., Charlot S., Tremonti C., Brinkmann J., 2004, MNRAS, 353, 713
Kawinwanichakij L. et al., 2017, ApJ, 847, 134
Kereš D., Katz N., Fardal M., Davé R., Weinberg D. H., 2009, MNRAS, 395, 160
Köppen J., Jáchym P., Taylor R., Palouš J., 2018, MNRAS, 479, 4367
Koribalski B. S. et al., 2018, MNRAS, 478, 1611
Kravtsov A., Manwadkar V., 2022, MNRAS, 514, 2667
Kuijken K. et al., 2019, A&A, 625, A2
Larson R. B., Tinsley B. M., Caldwell C. N., 1980, ApJ, 237, 692
Łokas E. L., Mamon G. A., 2001, MNRAS, 321, 155
Lotz M., Remus R.-S., Dolag K., Biviano A., Burkert A., 2019, MNRAS, 488, 5370
Maier C., Ziegler B. L., Haines C. P., Smith G. P., 2019, A&A, 621, A131
Mao Y.-Y., Geha M., Wechsler R. H., Weiner B., Tollerud E. J., Nadler E. O., Kallivayalil N., 2021, ApJ, 907, 85
Marinacci F. et al., 2018, MNRAS, 480, 5113
Martig M., Bournaud F., Teyssier R., Dekel A., 2009, ApJ, 707, 250
Mayer L., Mastropietro C., Wadsley J., Stadel J., Moore B., 2006, MNRAS, 369, 1021
McCarthy I. G., Frenk C. S., Font A. S., Lacey C. G., Bower R. G., Mitchell N. L., Balogh M. L., Theuns T., 2008, MNRAS, 383, 593
McConnachie A. W., 2012, AJ, 144, 4
McGaugh S. S., Schombert J. M., 2014, AJ, 148, 77
McQuinn K. B. W. et al., 2010a, ApJ, 721, 297
McQuinn K. B. W. et al., 2010b, ApJ, 724, 49
Moster B. P., Naab T., White S. D. M., 2013, MNRAS, 428, 3121
Moster B. P., Naab T., Lindström M., O'Leary J. A., 2021, MNRAS, 507, 2115
Moutard T., Sawicki M., Arnouts S., Golob A., Malavasi N., Adami C., Coupon J., Ilbert O., 2018, MNRAS, 479, 2147
Muratov A. L., Kereš D., Faucher-Giguère C.-A., Hopkins P. F., Quataert E., Murray N., 2015, MNRAS, 454, 2691
Naiman J. P. et al., 2018, MNRAS, 477, 1206
Navarro J. F., Frenk C. S., White S. D. M., 1996, ApJ, 462, 563
Nelson D. et al., 2018, MNRAS, 475, 624
Nelson D. et al., 2019, MNRAS, 490, 3234
Nichols M., Bland-Hawthorn J., 2011, ApJ, 732, 17
Oh S.-H. et al., 2015, AJ, 149, 180
Oñorbe J., Boylan-Kolchin M., Bullock J. S., Hopkins P. F., Kereš D., Faucher-Giguère C.-A., Quataert E., Murray N., 2015, MNRAS, 454, 2092
Ott J. et al., 2012, AJ, 144, 123
Pandya V. et al., 2021, MNRAS, 508, 2979
Papastergis E., Cattaneo A., Huang S., Giovanelli R., Haynes M. P., 2012, ApJ, 759, 138
Papovich C. et al., 2018, ApJ, 854, 30

Downloaded from https://academic.oup.com/mnras/article/528/1/365/7511121 by guest on 08 December 2024

Pearson S. et al., 2016, MNRAS, 459, 1827
Peñarrubia J., Navarro J. F., McConnachie A. W., 2008, ApJ, 673, 226
Peng Y., Maiolino R., Cochrane R., 2015, Nature, 521, 192
Penny S. J., Pimbblet K. A., Conselice C. J., Brown M. J. I., Grützbauch R., Floyd D. J. E., 2012, ApJ, 758, L32
Petts J. A., Gualandris A., Read J. I., 2015, MNRAS, 454, 3778
Pillepich A. et al., 2018a, MNRAS, 473, 4077
Pillepich A. et al., 2018b, MNRAS, 475, 648
Pillepich A. et al., 2019, MNRAS, 490, 3196
Planck Collaboration et al., 2016, A&A, 594, A13
Popping G., Behroozi P. S., Peeples M. S., 2015, MNRAS, 449, 477
Portinari L., Sommer-Larsen J., Tantalo R., 2004, MNRAS, 347, 691
Reddick R. M., Wechsler R. H., Tinker J. L., Behroozi P. S., 2013, ApJ, 771, 30
Roberts I. D., Parker L. C., Brown T., Joshi G. D., Hlavacek-Larrondo J., Wadsley J., 2019, ApJ, 873, 42
Rocha M., Peter A. H. G., Bullock J., 2012, MNRAS, 425, 231
Rodriguez-Gomez V. et al., 2015, MNRAS, 449, 49
Rodríguez-Puebla A., Primack J. R., Avila-Reese V., Faber S. M., 2017, MNRAS, 470, 651
Rodriguez Wimberly M. K., Cooper M. C., Fillingham S. P., Boylan-Kolchin M., Bullock J. S., Garrison-Kimmel S., 2019, MNRAS, 483, 4031
Roediger E., Hensler G., 2005, A&A, 433, 875
Sales L. V., Wang W., White S. D. M., Navarro J. F., 2013, MNRAS, 428, 573
Samuel J., Wetzel A., Santistevan I., Tollerud E., Moreno J., Boylan-Kolchin M., Bailin J., Pardasani B., 2022, MNRAS, 514, 5276
Sand D. J., Spekkens K., Crnojević D., Hargis J. R., Willman B., Strader J., Grillmair C. J., 2015, ApJ, 812, L13
Sand D. J. et al., 2022, ApJ, 935, L17
Schlafly E. F., Finkbeiner D. P., 2011, ApJ, 737, 103
Schlegel D. J., Finkbeiner D. P., Davis M., 1998, ApJ, 500, 525
Schreiber C. et al., 2018, A&A, 618, A85
Scoville N. et al., 2017, ApJ, 837, 150
Sheth R. K., Mo H. J., Tormen G., 2001, MNRAS, 323, 1
Simons R. C. et al., 2020, ApJ, 905, 167
Slater C. T., Bell E. F., 2014, ApJ, 792, 141
Somerville R. S. et al., 2018, MNRAS, 473, 2714
Springel V. et al., 2018, MNRAS, 475, 676
Stierwalt S., Besla G., Patton D., Johnson K., Kallivayalil N., Putman M., Privon G., Ross G., 2015, ApJ, 805, 2
Taylor E. N. et al., 2011, MNRAS, 418, 1587
Tonnesen S., 2019, ApJ, 874, 161
Tonnesen S., Bryan G. L., 2009, ApJ, 694, 789
Tremmel M. et al., 2019, MNRAS, 483, 3336
Trussler J., Maiolino R., Maraston C., Peng Y., Thomas D., Goddard D., Lian J., 2020, MNRAS, 491, 5406
Tully R. B. et al., 2006, AJ, 132, 729
Wadsley J. W., Stadel J., Quinn T., 2004, New A, 9, 137
Wang P., Abel T., 2008, ApJ, 672, 752
Wang L. et al., 2016, MNRAS, 458, 1450
Wang Y., Nadler E. O., Mao Y.-Y., Adhikari S., Wechsler R. H., Behroozi P., 2021, ApJ, 915, 116
Weinberger R. et al., 2017, MNRAS, 465, 3291
Weisz D. R. et al., 2011, ApJ, 739, 5
Weisz D. R., Dolphin A. E., Skillman E. D., Holtzman J., Gilbert K. M., Dalcanton J. J., Williams B. F., 2014, ApJ, 789, 148
Weisz D. R., Dolphin A. E., Skillman E. D., Holtzman J., Gilbert K. M., Dalcanton J. J., Williams B. F., 2015, ApJ, 804, 136
Wetzel A. R., Tinker J. L., Conroy C., 2012, MNRAS, 424, 232
Wetzel A. R., Tollerud E. J., Weisz D. R., 2015, ApJ, 808, L27
Wheeler C., Phillips J. I., Cooper M. C., Boylan-Kolchin M., Bullock J. S., 2014, MNRAS, 442, 1396
Woo J. et al., 2013, MNRAS, 428, 3306
Zentner A. R., Bullock J. S., 2003, ApJ, 598, 49
Zou H., Gao J., Zhou X., Kong X., 2019, ApJS, 242, 8
Zu Y., Mandelbaum R., 2016, MNRAS, 457, 4360

APPENDIX A: UTILIZING PROJECTED QUANTITIES

In the past it has been common to use projected quantities of the observed system, such as the 2D separation and line-of-sight velocity difference, to further constrain the set of analogues (e.g. Sales et al. 2013; Besla et al. 2018; Garling et al. 2020). This is typically implemented with Monte Carlo rejection sampling, where random rotation matrices are sampled and applied to the 3D positions and velocities of simulated subhaloes before calculating projected quantities along a chosen axis of observation. If these projected quantities match some set selection range, the subhalo is saved for later analysis. This procedure produces a better set of subhalo analogues because the projected quantities of the system we observe are correlated with their 3D quantities and thus contain useful information about the system. However, rejection sampling is a suboptimal method for this calculation. It is computationally inefficient, as a large portion of the samples are discarded on each iteration, and it is prone to numerical error when the sample size itself is small, as may be the case when working with small simulation volumes or very specific analogue selections. To avoid these issues, we derive directly the probabilities of subhaloes with given 3D positions and velocities having specific projected quantities. We first consider the projected separation.

Random observation of a host-subhalo system is equivalent to stating that the host-centric coordinate axes are randomly aligned with respect to our observation point; i.e. in spherical coordinates, the ϕ (polar angle) and θ (azimuthal angle) coordinates of the subhalo are uniformly distributed over the sphere. However, the host-centric distance of the subhalo is fixed (r in spherical coordinates). If we choose to observe along the Cartesian z-axis, we find a joint PDF of

$$\frac{\mathrm{d}P(x,\phi,\theta|r)}{\mathrm{d}x\,\mathrm{d}\phi\,\mathrm{d}\theta} = \frac{1}{4\pi}\,\mathrm{Sin}\,(\phi)\,\delta\left(r\sqrt{[\mathrm{Sin}\,(\phi)\,\mathrm{Cos}\,(\theta)]^2+[\mathrm{Sin}\,(\phi)\,\mathrm{Sin}\,(\theta)]^2}-x\right) \tag{A1}$$

where $\delta(X)$ is the Dirac delta function and x is the projected separation between the host and satellite. Marginalization over ϕ and θ gives the PDF for x given r,

$$\frac{\mathrm{d}P(x|r)}{\mathrm{d}x} = \frac{x\,\boldsymbol{\Theta}\,(r-x)}{r^2\sqrt{1-\frac{x^2}{r^2}}}, \tag{A2}$$

where $\boldsymbol{\Theta}(X)$ is the Heaviside function, which is 0 when $X<0$ and 1 when $X>0$. The PDF diverges as $\lim_{x\to r}\frac{\mathrm{d}P(x|r)}{\mathrm{d}x}=\infty$, though its integrated probability is finite with $\int_0^r\frac{\mathrm{d}P(x|r)}{\mathrm{d}x}\,\mathrm{d}x=1$. Given a PDF for the observed value of x given the data $\mathcal{D}$, denoted $\frac{dP(x|\mathcal{D})}{dx}$, the probability that a random observation of a subhalo with host-centric distance r is consistent with the observation is

$$\begin{aligned}P(x|r) &= \int_0^\infty \frac{x\,\boldsymbol{\Theta}\,(r-x)}{r^2\sqrt{1-\frac{x^2}{r^2}}}\,\frac{\mathrm{d}P(x|\mathcal{D})}{\mathrm{d}x}\,\mathrm{d}x\\ &= \int_0^r \frac{x}{r^2\sqrt{1-\frac{x^2}{r^2}}}\,\frac{\mathrm{d}P(x|\mathcal{D})}{\mathrm{d}x}\,\mathrm{d}x.\end{aligned} \tag{A3}$$

Though we find no position uncertainties for NGC 3109 in the literature, determining the centre of such a dwarf irregular is difficult and cannot be done to infinite precision. We adopt a Gaussian distribution for $\frac{\mathrm{d}P(x|\mathcal{D})}{\mathrm{d}x}$ with $\sigma=1$ kpc as an upper limit to the uncertainty.

We next consider the line-of-sight velocity difference (Δv) between satellite and the host. The velocity problem can be thought of

Downloaded from https://academic.oup.com/mnras/article/528/1/365/7511121 by guest on 08 December 2024

analogueously to the position problem; the magnitude of a subhalo's 3D velocity difference from its host is fixed, but the orientation of the velocity vector with respect to our observational axis is random. For a subhalo with a velocity difference vector $\boldsymbol{V} = \boldsymbol{V}_{\rm sat} - \boldsymbol{V}_{\rm host}$ with norm $|\boldsymbol{V}| = V$, the probability of measuring a line-of-sight velocity Δv is uniform from $-V$ to V, such that $\frac{{\rm d}P(\Delta v|V)}{{\rm d}\Delta v} = \boldsymbol{\Theta}\left(V - |\Delta v|\right)/2V$. If the data, $\mathcal{D}$, include some uncertainty on the observational line-of-sight velocity difference described by the PDF $\frac{{\rm d}P(\Delta v|\mathcal{D})}{{\rm d}\Delta v}$, we can write the probability that a random observation of $\boldsymbol{V}$ will match the observed value as

$$P(\Delta v|V) = \frac{1}{2V}\int_{-V}^{V}\frac{{\rm d}P(\Delta v|\mathcal{D})}{{\rm d}\Delta v}\,{\rm d}\Delta v. \tag{A4}$$

If $\frac{dP(\Delta v|\mathcal{D})}{d\Delta v}$ is Gaussian with mean μ and standard deviation σ, then

$$P(\Delta v|V) = \frac{1}{4V}\left[{\rm Erf}\left(\frac{V-\mu}{\sqrt{2}\,\sigma}\right) + {\rm Erf}\left(\frac{V+\mu}{\sqrt{2}\,\sigma}\right)\right]. \tag{A5}$$

We take the measured line-of-sight velocities and uncertainties from Table 1 for μ and σ. The probabilities are then multiplied into the weights from equation (5) as

$$\begin{aligned} w_i =& P(M_{h,{\rm sat},i}|M_{*,{\rm sat}})\; P(M_{h,{\rm host},i}|M_{*,{\rm host}}) \\ & P(x|r)\; P(\Delta v|V). \end{aligned} \tag{A6}$$

APPENDIX B: GAS MASS EVOLUTIONS FOR ALTERNATE MASS-LOADING FACTORS

We present here absolute gas mass evolutions for our simulated Antlia and Antlia B analogues (analogueous to Fig. 7) under the effects of both RPS and starvation, but with alternate models for the mass-loading factors. In Fig. B1, we show the absolute gas mass evolutions for Antlia B and Antlia analogues using the mass-loading factors from Muratov et al. (2015) which are about a factor of 10 greater than the fiducial Christensen et al. (2016) values. This leads to significantly reduced quenching times, necessitating more recent infalls (generally 1–2 Gyr ago) for the satellites in order to reproduce their present day measured H I masses. In contrast, Fig. B2 shows analogueous results but for a constant mass-loading factor of 1, as is sometimes used in semi-analytic calculations. In this case, the quenching time-scales are much longer than in the fiducial case, necessitating earlier infalls for the satellites in order to match their measured present-day H I masses. Both alternate mass-loading factors require infall times that are less likely for our sample than the fiducial Christensen et al. (2016) mass-loading factors (see Fig. 3).

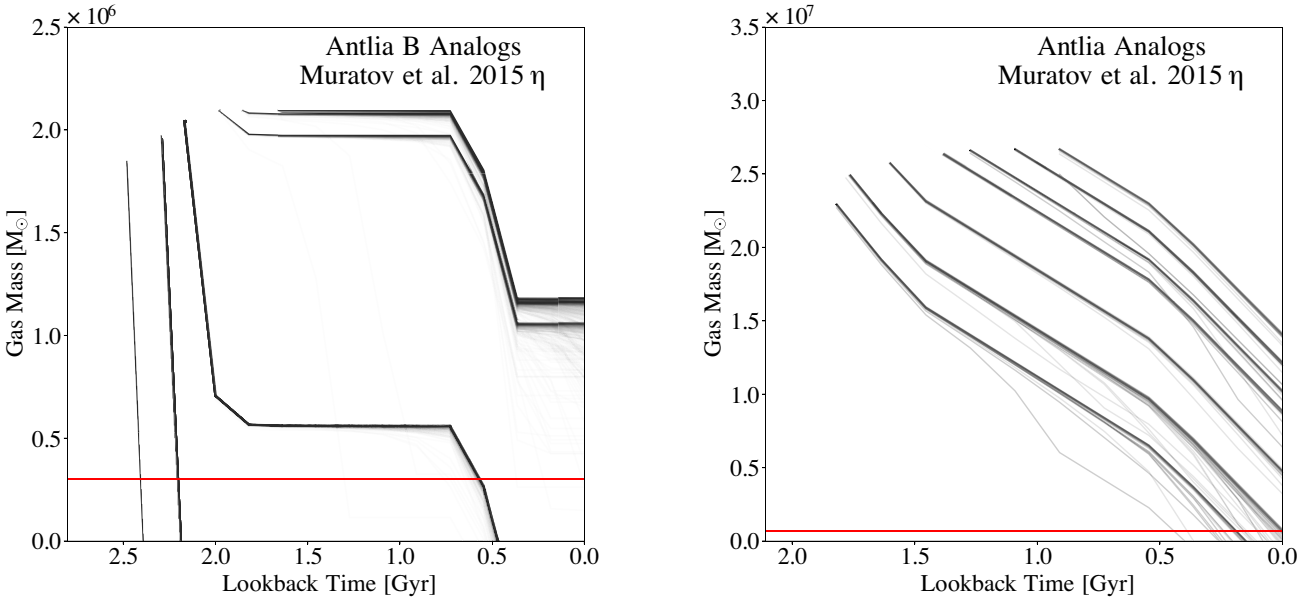

Figure B1. The total gas mass evolution including RPS and starvation for Antlia B (left) and Antlia (right) analogues with infall times between 1 and 2 Gyr ago computed with the Muratov et al. (2015) mass-loading factors. These mass-loading factors are about a factor of 10 higher than the fiducial Christensen et al. (2016) mass-loading factors, leading to much shorter quenching time-scales due to starvation. The weighted median infall times for the Antlia and Antlia B analogue samples are both about 4 Gyr, considerably earlier than required by this outflow model. The red horizontal lines mark the observed H I masses of Antlia and Antlia B, respectively (see Table 1).

Downloaded from https://academic.oup.com/mnras/article/528/1/365/7511121 by guest on 08 December 2024

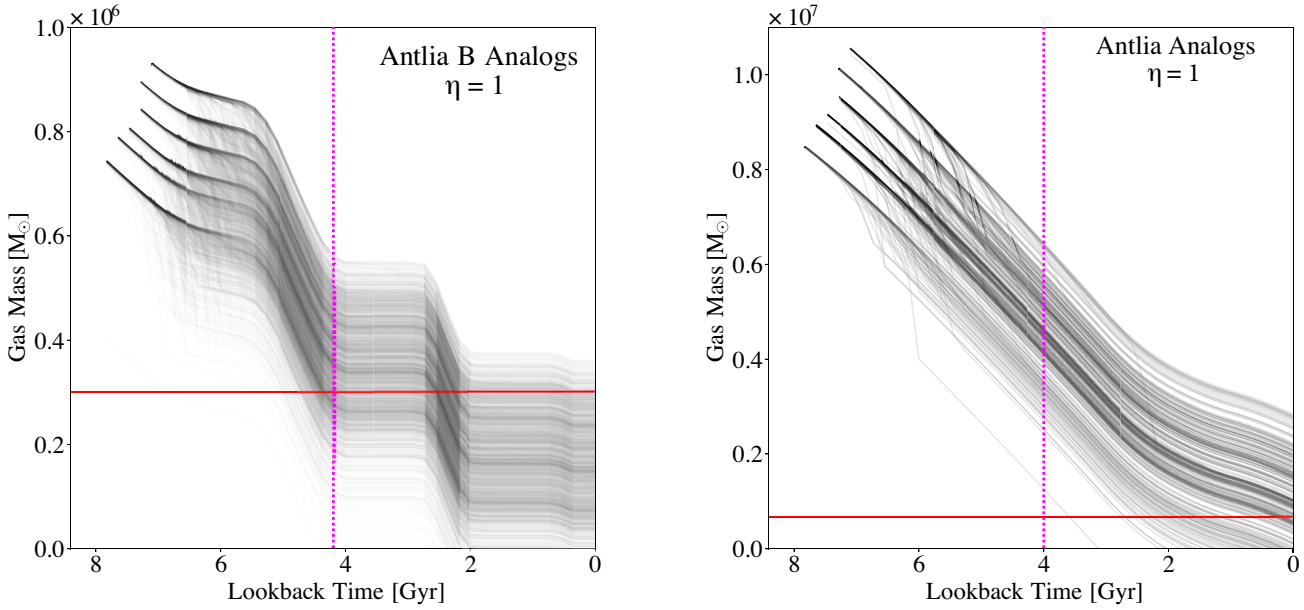

Figure B2. The total gas mass evolution including RPS and starvation for Antlia B (left) and Antlia (right) analogues with infall times between 7 and 8 Gyr ago computed with constant mass-loading factors of 1. These infall time bins were chosen to produce present-day satellite gas masses that are consistent with the observations. The red horizontal lines mark the observed present-day H I masses of Antlia and Antlia B, respectively (see Table 1). A mass-loading factor of unity is sometimes used in semi-analytic calculations, but requires very early infall times for Antlia and Antlia B; the weighted median infall times for the analogue satellite populations are indicated by vertical magenta dashed lines as in Fig. 3.

This paper has been typeset from a TEX/LATEX file prepared by the author.

Downloaded from https://academic.oup.com/mnras/article/528/1/365/7511121 by guest on 08 December 2024

© 2024 The Author(s).
Published by Oxford University Press on behalf of Royal Astronomical Society. This is an Open Access article distributed under the terms of the Creative Commons Attribution License (https://creativecommons.org/licenses/by/4.0/), which permits unrestricted reuse, distribution, and reproduction in any medium, provided the original work is properly cited.